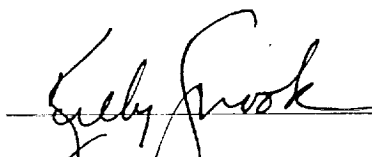
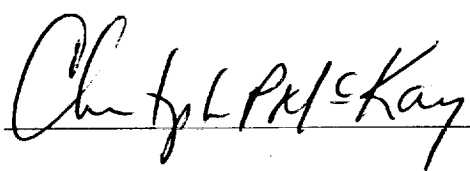


11-91  
371992

# Analysis of Physical Properties of Dust Suspended in the Mars Atmosphere

Summary of Work Performed  
for NASA Ames-Stanford Consortium NCC-5166  
October 1, 1995 - September 30, 1997

  
\_\_\_\_\_  
Kelly Snook, Stanford University

  
\_\_\_\_\_  
NASA Ames Co-Investigator - Chris McKay  
Stanford Principal Investigator - Brian Cantwell

20 August, 1998

SEP 14 1998  
To: CASI

## 1. Abstract

Methods for iteratively determining the infrared optical constants for dust suspended in the Mars atmosphere are described. High quality spectra for wavenumbers from 200 to 2000  $\text{cm}^{-1}$  were obtained over a wide range of view angles by the Mariner 9 spacecraft, when it observed a global Martian dust storm in 1971-2. In this research, theoretical spectra of the emergent intensity from Martian dust clouds are generated using a 2-stream source-function radiative transfer code. The code computes the radiation field in a plane-parallel, vertically homogeneous, multiply scattering atmosphere. Calculated intensity spectra are compared with the actual spacecraft data to iteratively retrieve the optical properties and opacity of the dust, as well as the surface temperature of Mars at the time and location of each measurement. Many different particle size distributions are investigated to determine the best fit to the data. The particles are assumed spherical and the temperature profile was obtained from the  $\text{CO}_2$  band shape. Given a reasonable initial guess for the indices of refraction, the searches converge in a well-behaved fashion, producing a fit with error of less than 1.2 K (rms) to the observed brightness spectra. The particle size distribution corresponding to the best fit was a lognormal distribution with a mean particle radius,  $r_m = 0.66 \mu\text{m}$ , and variance,  $\sigma^2 = 0.412$  ( $r_{eff} = 1.85 \mu\text{m}$ ,  $\nu_{eff} = .51$ ), in close agreement with the size distribution found to be the best fit in the visible wavelengths in recent studies. The optical properties and the associated single scattering properties are shown to be a significant improvement over those used in existing models by demonstrating the effects of the new properties both on heating rates of the Mars atmosphere and in example spectral retrieval of surface characteristics from emission spectra.

## 2. Methods

The goal of this work was to invert the Mariner 9 spacecraft data directly to determine the optical properties of the dust suspended in the Mars atmosphere.

To try to match any given Mariner 9 observation, we must know or estimate several things about the environmental conditions at the time of each measurement. The Mie and radiative transfer routines require these to be known in order to calculate brightness temperatures from given indices of refraction. Specifically, we must know the Martian surface temperature, the atmospheric temperature and pressure profiles, the dust optical depth and vertical mixing, and the dust particle shape and size distribution. None of these was independently measured at the time that the IRIS data were taken, so all must be inferred or estimated from the data, the literature or later spacecraft observations.

### 2.1 Overview of Solution Technique

Figure 2.3 illustrates the procedure used to iteratively determine the indices of refraction of the dust. Briefly, an initial guess for the imaginary index of refraction as a function of wavelength is made. A Kramers-Kronig routine is used to calculate the corresponding real indices of refraction. A lognormal particle size distribution is assumed for each data set and single scattering albedos are calculated using the Mie code. A multilayer radiative transfer code is called to calculate the theoretical brightness temperature of the emergent radiation for each orbit. Atmospheric temperature profiles are taken from previously inverted CO<sub>2</sub> bands in the Mariner 9 spectra, and we assume that the mixing ratio of the dust is uniform. Particle mean radius and the variance of the distribution are adjusted by finding the parameters corresponding to the closest fit in the 550 cm<sup>-1</sup> band of the data for all orbits. The temperature of the Martian surface and the optical depth for each orbit are adjusted by fitting the maximum transmission point (the wavenumber for which there is minimum absorption nor refraction) and the point of maximum absorption respectively. After the spectrum-specific parameters have been adjusted by fitting

appropriate regions of the spectra generated by the initial guess of optical properties with the spacecraft data, the optical properties themselves are then adjusted until the brightness temperature matches the data at all wavelengths and for all orbits.

The new optical properties are then made self-consistent using the Kramers-Kronig relations, and the entire process of adjustment is repeated until a set of self-consistent optical properties, particle size distribution, surface temperatures, temperature profiles, and optical depths is obtained.

In this chapter we describe in detail the theory and computational procedures that allow us to do what was just described.

## 2.2 Physical Model

This section explains the relationship between the optical properties of the Mars dust, the physical parameters associated with the environment, and the intensity of thermal emission observed by an orbiting instrument.

We begin with an introduction to the basic problem. As a radiation field propagates through an atmosphere, it is modified by various physical processes. In this work, we seek to isolate and study the interaction of atmospheric dust with the thermal emission in order to infer certain physical properties of the surface and dust particles. The molecular composition and the presence of aerosols such as dust or ice define the absorption and scattering properties of the atmosphere, which, combined with its thermal structure, determine the rate at which an atmosphere emits radiation at each wavelength in the thermal infrared.

Although our method of inverting the data is unique and new, we use previously well-established physical and computational methods to determine the radiative intensity emitted from the top of a plane parallel multiply scattering atmosphere [Toon *et al.*, 1977, Toon *et al.*, 1989, Goody and Yung, 1994], for the Mie single scattering theory which relates the optical properties of a spherical particle to its scattering properties, and for the relationship between the real and imaginary parts of the refractive index of a material [Hansen and Travis, 1974, Van de Hulst, 1971, Bohren and Huffman, 1983]. Here we review the physics of atmospheric radiative transfer and models used, and then outline our method of calling on these models

iteratively.

Several process modify the radiation field as it passes through a dust laden atmosphere along a particular line of sight of an observer in orbit. First is the emission from the surface of the planet, which we assume to be radiating as a blackbody. This radiation is attenuated as it passes through the atmosphere due to extinction (absorption plus scattering out of the path) by particles in the path. Second is the emission of the dust particles themselves which are in the line of sight between the spacecraft and the ground. These particles are radiating with an emissivity that varies with wavelength and this radiation is also attenuated by the fraction of the atmosphere between the particle and the spacecraft. Lastly, for a scattering atmosphere, radiation from elsewhere in the atmosphere (other particles, other places on the ground, etc.) is scattered into the line of sight by particles in the path. The spacecraft measures the sum of all these intensities to obtain a total intensity as a function of wavenumber at that particular view angle.

Here we shall briefly examine the general solution of the governing equation term by term to illustrate the above mentioned processes.

Consider a plane parallel atmosphere. Here we define for convenience the vertical optical depth,  $\tau$ , which can be thought of as the optical cross section of a unit area of height  $dz$ ,

$$d\tau = -N_o r_{eff} dz, \quad (2.1)$$

where  $N_o$  is the total number of dust particles in the column and  $r_{eff}$  is the effective optical crossection of the particles. Note that the sign in this definition means that the optical depth goes from zero at the top of the atmosphere, to  $\tau$  at the bottom, with  $z$  defined as shown. The equation of transfer for an arbitrary, monochromatic field of radiation is then given by

$$\begin{aligned} \mu \frac{dI(\tau_\nu, \mu, \phi)}{d\tau_\nu} = & I(\tau_\nu, \mu, \phi) \\ & - (1 - \varpi) B_\nu(T) \\ & - \frac{\varpi}{4\pi} \int_0^{2\pi} \int_{-1}^{+1} p(\mu, \phi; \mu', \phi') I(\tau_\nu, \mu', \phi') d\mu' d\phi' \end{aligned} \quad (2.2)$$

where  $\Theta$  is the angle between the directions of incidence,  $(\mu, \theta)$ , and scattering  $(\mu', \theta')$ ,  $p$  is the phase function for single scattering, defined as the angular distribution of radiation scattered once through the angle  $\Theta$ , and  $\varpi$  is the albedo for single scattering, defined as the ratio of radiant power scattered in all directions to that extinguished, or

$$\varpi = \int_0^{4\pi} p(\mu', \phi'; \mu, \phi) \frac{d\omega'}{4\pi}. \quad (2.3)$$

Physically,  $\varpi$  can be interpreted as the probability that a photon intercepted by a particle is scattered by that particle.

The subscript  $\nu$  will heretofore be dropped for ease of notation, but it should remain understood that all parameters, in general, are functions of  $\nu$ . We assume azimuthal symmetry, implying that there are no horizontal gradients in atmospheric properties, so the dependence on  $\phi$  is eliminated.

Our formal solution for the upward intensity emitted in the direction  $(\mu)$  from the top of the atmosphere is, term by term:

$$\begin{aligned} I(\tau, \mu) = & \\ (1) & \quad I(\tau_*, \mu) e^{-\tau_*/\mu} \\ (2) & + \int_0^{\tau_*} (1 - \varpi) e^{-\tau'/\mu} B(\tau') d\frac{\tau'}{\mu} \\ (3) & + 2\pi \int_0^{\tau_*} \int_{-1}^{+1} e^{-\tau'/\mu} p(\mu; \mu') I(\tau', \mu') d\frac{\tau'}{\mu} \\ (4) & + \frac{F_o \mu}{4\pi} \int_0^{\tau_*} e^{-\tau'/\mu_o} e^{-\tau'/\mu} p(\mu; -\mu_o) d\frac{\tau'}{\mu} \end{aligned} \quad (2.4)$$

where the numbered terms represent:

1. radiation originating from the planet's surface, attenuated by extinction as it passes through the dust column of vertical optical depth,  $\tau_*$  in the direction of  $\mu$ .
2. radiation originating from a volume of emitting dust particles at a level  $\tau'$ , attenuated by the column of dust above the volume
3. radiation from all directions  $\mu'$ , scattered one or more times into the direction  $\mu$  by a volume of particles at a level  $\tau'$ , attenuated by the column of dust

above the volume

4. radiation from the sun that has penetrated to depth  $\tau'$  and has been scattered back into the line of sight

Note that the Planck function  $B$  is written  $B(\tau)$  to emphasize that temperature is a function of optical depth alone (not  $x$  or  $y$ ) in plane-parallel atmospheres. In this work, we neglect the last term (the solar term) because the solar flux in infrared wavelengths is negligible compared to the planetary radiation.

Using approximations for the scattered intensity field and the scattering phase function in term 3, and employing the appropriate boundary conditions, the above equation is numerically integrated to calculate the upward intensity leaving the top of the atmosphere, given a particular set of surface and atmospheric temperatures, and given information about the absorbing and scattering properties of the atmosphere. Further, a vertically non-homogeneous atmosphere can be modelled by stacking individual layers and using the upward intensity from top of a lower layer as the boundary condition for the intensity entering the bottom of the layer above it. This stacking of layers will be discussed later in the section describing the multilayer code.

The particles of dust in the atmosphere are of a diameter comparable to the wavelenths of radiation with which they interact. These particles are large enough to contain an optical ray, and we must treat all effects of diffraction, refraction, reflection, and phase shifts of the radiation as it passes through and around each particle. To relate the dust's intrinsic material properties to its radiative scattering properties, we use the method of Mie [1908], which is an exact solution of the scalar wave equation in spherical coordinates

$$\frac{1}{r} \frac{\partial^2(r\psi)}{\partial r^2} + \frac{1}{r^2 \sin \theta} \frac{\partial}{\partial \theta} \left( \sin \theta \frac{\partial \psi}{\partial \theta} \right) + \frac{1}{r^2 \sin^2 \theta} \frac{\partial^2 \psi}{\partial \phi^2} + k^2 \psi = 0, \quad (2.5)$$

where the propagation constant,  $k$  is given by

$$k = (\varepsilon \mu \omega^2 + i \sigma \mu \omega)^{1/2} = \frac{\omega}{c} (n_r + i n_i). \quad (2.6)$$

Linear combinations of the resulting vector fields satisfy Maxwell's equations. For a detailed treatment of the Mie theory, we refer the reader to any radiative transfer text [eg, Van de Hulst, 1957]. The Mie theory requires only that the particles be spherical, which is a good, but not perfect, assumption for the dust aerosols.

The scattering properties we wish to calculate using the Mie theory are defined by the efficiency of the particles to scatter and absorb radiation. A particle of radius  $r$  has a geometric crosssection,  $\sigma_g$  of  $\pi r^2$ , and a wavelength-dependent "crosssections" for extinction, absorption, and scattering,  $\sigma_{ext}$ ,  $\sigma_{abs}$ , and  $\sigma_{sct}$ , respectively. These optical crosssections can be thought of physically as the crosssection of a particle that an incident wave of wavelength  $\lambda$  sees, which may or may not be the same as the geometric crosssection. We then define the efficiencies for extinction, absorption, and scattering as

$$\begin{aligned} Q_{ext} &= \frac{\sigma_{ext}}{\sigma_g} \\ Q_{abs} &= \frac{\sigma_{abs}}{\sigma_g} \\ Q_{sct} &= \frac{\sigma_{sct}}{\sigma_g}. \end{aligned} \tag{2.7}$$

noting that extinction is the sum of absorption and scattering, so that

$$\begin{aligned} \sigma_{ext} &= \sigma_{abs} + \sigma_{sct} \\ Q_{ext} &= Q_{abs} + Q_{sct} \end{aligned}$$

According to Kirchoff's law, the absorption crosssection and efficiency factor of a particle are equal to its emission crosssection and efficiency.

The value of  $Q_{ext}$  is typically on the order of unity, but can range from very small ( $\ll 1$ ) if the radius of the particle is much smaller than the wavelength of incident radiation (Rayleigh regime), to up to 4 or more for non-absorbing particles when of large radius (geometric limit). Since the scattering and absorbing properties of a given material are so sensitive to the ratio of particle size to incident wavelength, a study of the behavior of  $Q$  as a function of this ratio sheds valuable insight into the choice of particle size distribution.



It is useful to define a size parameter,

$$x = \frac{2\pi r}{\lambda} \quad (2.8)$$

for use in discussing the behavior of  $Q_{\text{ext}}$ . The particles in a dusty planetary atmosphere are typically not of one uniform radius. Instead, there is a distribution of particle sizes with a probability function  $n(r)$ , with particles ranging in size in the case of Mars over several orders of magnitude ( $.001 \mu\text{m} \leq r \leq 100 \mu\text{m}$ ).

The single scattering albedo, defined earlier as the ratio of radiant energy scattered to that extinguished, can be expressed in terms of the scattering and extinction coefficients:

$$\omega = \frac{Q_{\text{scat}}}{Q_{\text{ext}}} \quad (2.9)$$

Finally, in discussing the scattering properties of a material, we would like to know something about the mean angle of scattering of a particle. This is represented by the asymmetry parameter,

$$g = \int_{4\pi} (\cos \theta) p(\cos \theta) \frac{d\Omega}{4\pi}, \quad (2.10)$$

where  $p(\cos \theta)$  is the phase function we mentioned earlier. The phase function is normalized and given by

$$\int_{4\pi} p(\cos \theta) \frac{d\Omega}{4\pi} = 1 \quad (2.11)$$

and describes the probability of a particle to scatter radiation into the direction  $\cos \theta$ . The asymmetry parameter, then, can have values between -1 and 1, where a value of +1 indicates that all radiation is scattered into the forward direction, a value of 0 indicates that radiation is scattered isotropically, and a value of -1 represents complete backscattering. Typical values for dust particles such as those found in the Mars atmosphere are  $0.1 < g < 0.8$ , with longer wavelengths being scattered more isothermally and shorter wavelengths being more forward scattered.

The relationship between scattering efficiency and total optical depth is simple

and conducive to a physical understanding of these parameters. We may write

$$\tau = N_o \sigma_g Q_{\text{ext}} \quad (2.12)$$

or we can consider the mass of a unit area column of atmosphere

$$\begin{aligned} M &= \int_0^\infty \left(\rho \frac{4}{3} \pi r^3\right) N n(r) dr \\ &= \frac{4}{3} \rho N r_{\text{eff}} \sigma_g \end{aligned} \quad (2.13)$$

where  $N$  is the total number particles of all sizes and  $\rho$  is the volumetric mass of a particle. We can then relate the optical depth and mass

$$\tau = \frac{3M Q_{\text{ext}}}{4\rho r_{\text{eff}}} \quad (2.14)$$

It is evident from equation 2.12 that since the number of particles,  $N$ , and the geometric crossection,  $\sigma_g$ , are independent of wavenumber, we can find the optical depth at any wavenumber if we know the extinction efficiency at that wavenumber by a simple scaling using  $Q_{\text{ext}}$  and  $\tau$  at a reference wavelength, or

$$\tau(\nu) = \frac{\tau(\nu = \nu_{\text{ref}})}{Q_{\text{ext}}(\nu = \nu_{\text{ref}})} Q_{\text{ext}}(\nu) \quad (2.15)$$

We make frequent use of this convenient scaling to compute  $\tau$  quickly at all wavelengths once it is known at a reference wavelength.

The temperatures of both the atmosphere and the surface greatly affect the intensity of the radiation being emitted from the top of the atmosphere. The relationship between these temperatures and the upward intensity is straightforward and intuitive, although the mathematical relationship is not linear or simple. Physically speaking, a warmer surface temperature will cause the brightness temperatures at all wavenumbers to increase, but there will be a more pronounced effect at wavenumbers for which the indices of refraction of the dust are small. At wavenumbers for which the dust is optically thick due to high indices of refraction, the surface temperature has less effect because the surface is obscured by the intervening atmosphere.

Conversely, the temperature profile in the atmosphere has the greatest effect inside the dust absorption bands in the spectrum, with the temperature at the top of the dust layer effecting the temperatures at the cores of the bands and temperatures farther down affecting the wings of the bands. Therefore, the thermal structure of the atmosphere and the temperature at which the surface is radiating are important parameters in any radiative transfer model. The temperatures manifest themselves in Equation 2.4 in the Planck functions that are used to describe the intensity of radiation coming from the surface, as well as in the Planck functions for the emitting particles suspended in the atmosphere.

One additional question we would like to answer concerns the overall heating or cooling effect of the suspended dust. A simple way to look at this to first order is to simply integrate the upward and downward intensities,  $I^+$  and  $I^-$ , which we have computed for each wavelength at specific emission angles, so that we may obtain a hemispherical mean flux quantity as a function of altitude, or

$$F^+(z) = \int_0^\infty \pi I^+ d\nu$$

$$F^-(z) = \int_0^\infty \pi I^- d\nu.$$

Qualitatively, we would expect the upward flux to decrease with height from a value of  $\sigma T^4$  at the surface to a somewhat smaller value at the top of the atmosphere. The downward fluxes also decrease but are much smaller in magnitude since they are due solely to downward scattering of radiation. These downward fluxes are zero at the top of the atmosphere and some small value at the surface.

In summary, the set of parameters,  $Q_{\text{ext}}$ ,  $\varpi$ ,  $g$ , constitute the scattering properties of a material. They are all dependent upon wavelength, and also vary strongly with particle size, shape, and composition. The Mie theory provides an exact relationship between the optical properties of a particle and the particle's absorption and extinction efficiencies. For a distribution of particles, an average set of efficiencies can be found by integrating over all particle radii. The scattering properties therefore appear in the radiative transfer equation in the form of  $\varpi$ ,  $\varepsilon$  (the emissivity,

which, by Kirchoff's Law, is given by

$$\varepsilon = (1 - \varpi), \quad (2.16)$$

and  $p(\cos \theta)$ . The optical properties,  $n_i$  and  $n_r$ , plus information about particle size, shape, and distribution are contained within these scattering properties. The wavelength-dependent optical depth of the atmosphere appears directly in the equation and can be computed at every wavelength using the scattering efficiency and one reference optical depth. Finally, the temperatures of the surface and atmosphere enter the radiative transfer equations inside the Planck functions for the surface (used in term (1) of Equation 2.4) and the emitting dust particles (term (2)). Overall heating effects of the dust can be examined by integration of upward and downward intensities over all wavelengths.

The reader should now have a basic idea of the main parameters effecting our analysis of the interaction between suspended Mars dust and the thermal infrared radiation field of the planet. This brings us to the detailed discussion of the model and the methods for determining the parameters and properties of interest.

## 2.3 Computational Models

We use an iterative procedure to determine the indices of refraction of the suspended Mars dust, optical depths of the atmosphere for each orbit, surface temperatures for each orbit, and the particle size distribution of the dust. A detailed flow diagram showing the various components of the procedure is shown in Figure 2.4. Atmospheric temperatures, surface emissivity, particle shape, and vertical mixing ratio are assumed to be known, and these assumptions will be discussed at length in following detailed descriptions of the model and procedures.

The major subroutines of the model are the Mie single-scattering code, which calls on the Mie theory for each particle size radius then computes average scattering properties for the dusty atmosphere; the Kramers-Kronig code used to compute physically consistent real indices of refraction for a set of imaginary indices; and the multilayer radiative transfer code which calculates the upward intensity of radiation

after it has passed through a vertically inhomogeneous, multiply scattering atmosphere by stacking individual layers of atmosphere and solving the radiative transfer equation for all layers simultaneously as a matrix of coupled equations.

Procedures for using the above models consist of two broad categories of fits. First, the particle size distribution, surface temperature, and optical depth are systematically varied, holding the indices of refraction constant at their initial guess, until the theoretical brightness temperature spectra generated by these parameters fit the data at specific wavenumbers. We refer to this process as the “adjustment” of particle size distribution, optical depth, and surface temperature.

The second broad category of fits involves holding all the parameters which have just been adjusted fixed and searching at each wavelength for indices of refraction that correspond to the best match of brightness temperature to the spacecraft data. This general process of fitting optical processes is sometimes referred to here as the “search”. Once new sets of optical properties are found, the real and imaginary indices must be re-correlated to each other using Kramers Kronig, which comprises the next initial guess of optical properties to be used by the adjustment routine.

The above procedure is iterated until the optical properties which come out of the final search routine match those which were input to the adjustment routine.

Now we will describe each computational model and procedure.

### 2.3.1 Mie Code

We have developed a driver program, called *xmie*, which calls a standard Mie code written at NASA Ames Research Center for every particle radius in a given particle size distribution at a given wavenumber. Subroutine *xmie* then integrates the scattering properties over all radii and divides by the appropriate normalization constant to obtain the average scattering properties for the layer of dust in question. It is capable of employing two different types of particle size distributions: the lognormal particle size distribution, which is the one we use in this thesis, and the modified gamma distribution [Diermendjian, 1969], which we can compute for comparison to previous work [Toon *et al.* , 1977, Clancy *et al.* , 1995, Ockert-Bell *et al.* , 1997, Pollack *et al.* , 1991].

### 2.3.1.1 Particle Size Distributions

The logarithmic normal particle size distribution is a useful model for many polydisperse populations in nature [Campbell, 1995]. It is the model chosen to represent the distribution of dust particles in the atmosphere of Mars in this work.

We assume the dust to be comprised of lognormally distributed particles for which the probability density function is

$$n(r)dr = \frac{1}{r\sigma(2\pi)^{1/2}} \exp \left[ -\frac{(\ln r - \mu)^2}{2\sigma^2} \right] d \ln r \quad (2.17)$$

where  $\mu$  and  $\sigma$  are the mean and variance of  $\ln(r)$  respectively. It is normalized such that

$$N(r) = \int_0^\infty n(r)dr = 1.0 \quad (2.18)$$

The distribution can be uniquely defined by the two parameters,  $\mu$  and  $\sigma^2$ , which describe logarithmic quantities and are therefore dimensionless. The notation of  $\sigma$  for the variance of particle size distribution is unfortunately similar to the notation we've chosen for the geometric and optical crosssections of the particles, but they should not be confused.

Given the average geometric particle size,  $\bar{\sigma} = \int_0^\infty \pi r^2 n(r)dr$ , the average extinction and scattering properties of the atmosphere can then be computed:

$$\left\{ \begin{array}{l} \bar{Q}_{\text{sct}} = \frac{\int_0^\infty \pi r^2 Q_{\text{sct}}(r)n(r)dr}{\int_0^\infty \pi r^2 n(r)dr} \\ \bar{Q}_{\text{abs}} = \frac{\int_0^\infty \pi r^2 Q_{\text{abs}}(r)n(r)dr}{\int_0^\infty \pi r^2 n(r)dr} \\ \bar{Q}_{\text{ext}} = \frac{\int_0^\infty \pi r^2 Q_{\text{ext}}(r)n(r)dr}{\int_0^\infty \pi r^2 n(r)dr} \end{array} \right. \quad (2.19)$$

Similarly,

$$\bar{g} = \frac{\int_0^\infty \pi r^2 g(r)n(r)dr}{\int_0^\infty \pi r^2 n(r)dr} \quad (2.20)$$

and

$$\varpi = \frac{Q_{\text{scat}}}{Q_{\text{ext}}}. \quad (2.21)$$

Figure 2.1 illustrates several lognormal distributions with different values of  $\mu$  and  $\sigma$ .

For verification of our integration of particle size distributions, we turning our attention to the moments of the probability function,

$$\bar{r}^n = \int_0^\infty r^n n(r) dr, \quad (2.22)$$

an analytical integration gives

$$\bar{r}^n = [r]^n e^{\sigma^2 n^2 / 2} \quad (2.23)$$

where  $n = 0, 1, 2, \dots$ , we have the following:

$$\begin{cases} n = 0 & \bar{r}^0 = 1 \\ n = 1 & \bar{r}^1 = [r] e^{\sigma^2 / 2} \\ n = 2 & \bar{r}^2 = [r]^2 e^{\sigma^2} \\ n = 3 & \bar{r}^3 = [r]^3 e^{9\sigma^2 / 2} \end{cases} \quad (2.24)$$

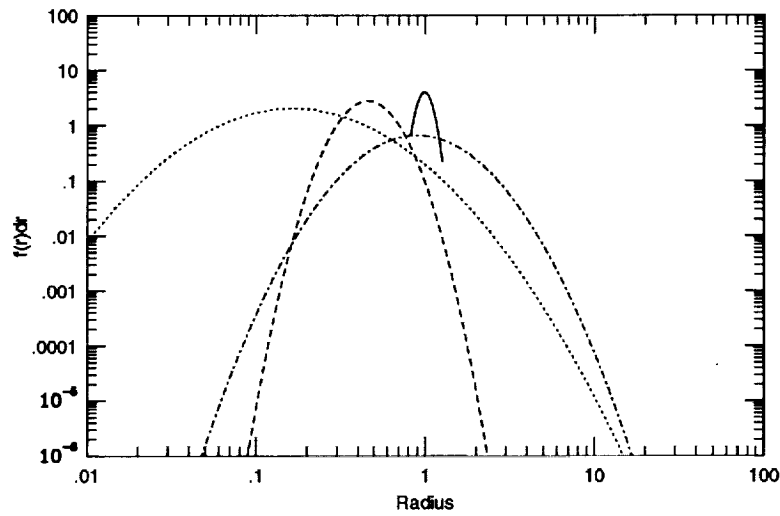
These yield median and mean values

$$\begin{cases} [r] = e^\mu & \text{median radius} \\ [s] = \pi [r]^2 & \text{median area} \\ [v] = 2\pi [r]^3 & \text{median volume} \end{cases} \quad (2.25)$$

$$\begin{cases} \langle r \rangle = \bar{r} & \text{mean radius} \\ \langle s \rangle = \pi \bar{r}^2 & \text{mean radius} \\ \langle v \rangle = 2\pi \bar{r}^3 & \text{mean volume} \end{cases} \quad (2.26)$$

The code used in this work computes the particle size distribution, given  $\mu$  and  $\sigma$  in subroutine `xmie`. At each particle radius, the effective radius and variance are computed, along with the single scattering properties returned by `xmie`, by

**Figure 2.1:** Four particle size distributions are shown here: The dotted line is  $r_0 = .33, \sigma = .8367$ , with  $r_{eff}$  and  $v_{eff}$  matching Clancy *et al.* [1995]; The dot-dashed line is  $r_0 = 1.23, \sigma = .5658$ , with  $r_{eff}$  and  $v_{eff}$  matching Toon *et al.* [1977]; The solid line is  $r_0 = 1, \sigma = .1$





integrating over  $0 \leq r \leq \infty$ . A gaussian quadrature routine, as described in Numerical Recipes [Press *et al.* 1996], pp. 121-125, is used to calculate the abscissas and weights at equal spacing in logspace for the integration. The analytical moments can be computed and compared with the integration to ensure accuracy. Using 100 gauss points, the computed integration agrees with the analytical moments to within  $10^{-7}$ .

It is common to see in the literature references to the particle “effective radius”, which is defined as the cross sectional area weighted radius, and a corresponding “effective variance”

$$\begin{cases} r_{eff} = \frac{\int_0^\infty r \pi r^2 n(r) dr}{\int_0^\infty \pi r^2 n(r) dr} = \frac{\bar{r}^3}{\bar{r}^2} \\ v_{eff} = \frac{\int_0^\infty r^2 \pi r^2 n(r) dr}{\int_0^\infty \pi r^2 n(r) dr} \end{cases} \quad (2.27)$$

For comparison to previous research, the model can employ a modified gamma distribution, given by

$$n(r) = C r^\alpha e^{-\frac{\alpha}{\gamma} (\frac{r}{r_m})^\gamma} \quad (2.28)$$

where  $r_m$  is the mode radius of the distribution,  $\alpha$  and  $\gamma$  are positive constants, and  $C$  is the normalization constant to ensure  $\int_0^\infty n(r) dr = 1$ .

The effective radius and effective variance,  $r_{eff}$  and  $v_{eff}$ , can be related analytically to the lognormal mean radius and variance [Forget, 1996],  $r_o$  and  $\sigma$ ,

$$\begin{aligned} r_o &= r_{eff} / (1 + v_{eff})^{(5/2)} \\ \sigma^2 &= \ln(1 + v_{eff}), \end{aligned} \quad (2.29)$$

and to the modified gamma parameters,  $r_m$ ,  $\alpha$ , and  $\gamma$ , by

$$\begin{aligned} r_{eff} &= r_m \left( \frac{\gamma}{\alpha} \right)^{1/\gamma} \frac{\Gamma(\frac{\alpha+4}{\gamma})}{\Gamma(\frac{\alpha+3}{\gamma})} \\ v_{eff} &= \frac{\Gamma(\frac{\alpha+5}{\gamma}) \Gamma(\frac{\alpha+3}{\gamma})}{\Gamma(\frac{\alpha+5}{\gamma})^2} - 1 \end{aligned} \quad (2.30)$$

where  $\Gamma$  is the Gamma function  $\Gamma(x) = \int_0^\infty t^{x-1} e^{-t} dt$ .

Although the lognormal and modified gamma distributions might look very

different from each other for the same values of  $r_{\text{eff}}$  and  $v_{\text{eff}}$ , Hansen and Travis [1974] showed that the average scattering properties depend very little on these differences and depend in most cases only on  $r_{\text{eff}}$  and  $v_{\text{eff}}$ .

Ideally we would like to find a particle size distribution that matches observed data for all wavelengths in the electromagnetic spectrum. Past studies have had difficulty finding particle size distributions that would match data both in the infrared and in the solar wavelengths. We seek in our model to find solutions for the optical properties using particle size distributions found by previous researchers to fit data in various wavelength regions [Toon *et al.* , 1977, Clancy *et al.* , 1991, Drossart *et al.* , 1991, Pollack *et al.* , 1995, Ockert-Bell *et al.* , 1997], and also to iteratively converge on a best fit of our own for comparison to these previously obtained particle size distributions. We show results for cases in which particle size and variance were held fixed and all other free parameters adjusted and fit to the data, as well as results for the case when we let our model find its own best particle size distribution.

### 2.3.2 Multilayer Radiative Transfer Code

We use the word “multilayer” to indicate that our radiative transfer code is capable of approximating a vertically inhomogeneous atmosphere by stacking a number of single, homogeneous layers atop one another and solving the set of coupled equations to calculate the emergent intensity at the top of the stack. We will briefly sketch out the problem here. The atmosphere is divided into  $n$  layers ( $n = 4$  here), numbered from top to bottom,  $j = 1, 4$ . Atmospheric temperatures and optical depths must be specified at each boundary, so they are numbered from 1 to  $n+1$ . Each layer is comprised of particles of particle size distribution  $n_j(r)$ . We can write for each layer four equations, one each for  $I_o^-$ ,  $I_o^+$ ,  $I_*^-$ ,  $I_*^+$ , and each layer has 6 unknowns. There are two equations of continuity between each layer, and two boundary conditions (one at the surface and one at the top of the top layer), therefore we have a total of  $4*n+4*2$  equations and the same number of unknowns, and we can solve directly for the intensity anywhere in the field.

The model is capable of considering vertical inhomogeneities in particle size distribution, atmospheric temperature gradient, and optical depth, but is not ca-

pable of modelling any inhomogeneities in the basic dust particle composition (ie indices of refraction). A detailed study of the effects of varying particle distribution spatially and temporally would be of great interest, but is beyond the scope of this thesis. We assume for the purposes of our study that the particle size distribution is spatially and temporally constant. That is, we assume that the relative abundance of large to small particles is the same at higher altitudes as it is at lower altitudes, and that this distribution does not change throughout the duration of the duststorm. Both of these assumptions are contrary to physical intuition. Spatially, one might imagine that it's very probable for larger particles to dominate the distribution at lower altitudes, and for smaller particles to dominate at higher altitudes, due to the tendency for particles to assume a vertical density profile according to the ratio of their potential energy to the thermal energy  $KT$  (where  $K$  is Boltzmann's constant and  $T$  is the local equilibrium temperature). For this natural vertical particle size profile not to occur, there must be enough turbulent mixing as to keep the particles uniformly distributed. We employ the conclusion by Toon *et al.* [1977] and Conrath *et al.* [1975] that Stokes Cunningham fallout is not the dominant mechanism leading to the dust storm clearing and that strong vertical mixing persisted throughout the duration of the storm. This assumption, although supported by some studies, is controversial [Haberle, private communication], and merits further study.

Although the size distribution of particles is assumed to be constant with height, the density of the particles is not. We assume a constant ratio of dust mass to atmospheric mass, so that the particles become less dense with height.

Table 2.1 gives list of physical parameters that must be specified to generate a synthetic spectrum.

Several assumptions and approximations are necessary to make the solution of the multilayer radiative transfer equation tractable. Briefly, the most important are

1. the representation of the radiation intensity field inside term (3) of Equation 2.4 as two streams of radiation, one in the positive (upward) direction and one in the negative (downward) direction,

**Table 2.1: Parameters used in solution of multilayer radiative transfer equation**

Symbol	Parameter	Specified by
$n_{layer}$	Number of layers	Choice
$nspec$	Number of spectra	Choice
$ndat$	Number of datapoints	Smoothed Mariner9 data
$n_i(ndat)$	Imaginary indices of refraction	Iterative bisection
$n_r(ndat)$	Real indices of refraction	Kramers-Kronig
$T_{surf}(nspec)$	Surface Temperatures	Iterative bisection
$T_i(n_{layer} + 1, nspec)$	Atmospheric Temperatures	CO <sub>2</sub> band inversion
$\tau_{ref}(n_{layer} + 1, nspec)$	Ref. Optical Depth, $\lambda = 9\mu m$	Iterative bisection
$r_m(n_{layer}, nspec)$	Particle mean radius	Step search
$\sigma(n_{layer}, nspec)$	Particle size dispersion	Step search
$e_{surf}(nspec)$	Surface emissivity	Assumed black=1.0

2. use of just the first terms of the legendre polynomial expansion of the phase function,  $p(\cos \theta)$ , also inside term (3),
3. use of just the first term of the Taylor expansion of  $B(\tau)$  in determining the Planck function in terms (1) and (2) of Equation 2.4, namely

$$B(\tau) = B_0 + B_1\tau \quad (2.31)$$

4. use of the approximate atmospheric temperature profiles inverted from the CO<sub>2</sub> band using the assumption that dust was not absorbing in that region
5. calculations and searches performed only at wavenumbers outside the major CO<sub>2</sub> absorption bands
6. the assumption that incoming solar radiation is negligible in the infrared, compared radiation from the Martian surface
7. the assumptions that the dust is well mixed from the ground up to a height where the atmospheric pressure is 0.1 mbar and that the mixing ratio of dust to atmosphere remains constant to that height, where the dust ends abruptly
8. the approximation that dust particles behave as spherical particles.

9. the approximation of surface emissivity of unity rather than having a spectrum of its own [Christensen *et al.* , 1997]

The multilayer code returns the upward radiation in the form of brightness temperature for comparison to the spacecraft data.

### 2.3.3 Searching routines

A number of searches are performed on various parameters to obtain the best fit to the data. Parameters for which searches are performed include the reference optical depths, the surface temperatures, the particle size distribution, and the optical properties themselves. In all cases except for the particle size distribution, the criterion for fitting is the square of the error between the computed and the actual brightness temperatures. For properties which are the same for all orbits (optical properties and particle size distribution), the square of the error is summed over all orbits. In all cases except for the optical properties, the error function, which we call  $\chi$ , is well behaved, and a simple bracketed bisection searching method is used, holding all other parameters besides the one sought constant and finding the value of the parameter of interest which generates the minimum error in brightness temperature.

#### 2.3.3.1 Particle Size Distribution

The particle size distribution is the only search which is not completely automated. Two separate loops stepping through a range of possible mean particle radii and variances are wrapped around the outside of the code, and the best particle size parameters are chosen after the rest of the searches have been carried out for each possible combination. This is a long and laborious process, which we often disable and instead pick a reasonable particle size distribution *a priori* based on the literature, and perform the subsequent searches on just that one set of particle size parameters.

#### 2.3.3.2 Surface Temperature and Tau

Surface temperature and reference optical depth are strongly coupled, so the process of searching on these parameters is a smaller iterative loop within the

larger “adjust” iteration. First, using the initial guess for optical properties at the wavenumber for which the brightness temperature is a maximum (discussed earlier as the wavenumber most sensitive to surface temperature), and using an initial guess for reference optical depth, holding all other parameters constant, the surface temperatures are found for each orbit which produce brightness temperatures that match the spacecraft data at that one maximum point in the curve. Then, using those new values for surface temperature and holding everything else constant, the reference optical depths are adjusted until the curves fit at the wavenumber in the core of the  $9\text{ }\mu\text{m}$  dust band. This fit causes the curves at the maximum brightness temperature point not to match anymore, so another search on surface temperature is done, and so on until both points fit exactly for all orbits. This iteration always converges as long as the initial guess for optical properties has at least a rough dust-like absorption feature, so that the brightness temperatures are more sensitive to the surface temperature than to optical depth at the maximum brightness temperature point, and less sensitive to surface temperature than to optical depth at the wavenumber corresponding to the core of the dust absorption feature in the data.

### 2.3.3.3 Indices of Refraction

The complex index of refraction is given by

$$n(\lambda) = n_r(\lambda) - m_i(\lambda) \quad (2.32)$$

where  $n_r$  is the usual refractive index which determines phase speed, and  $n_i$  is related to the absorption coefficient

$$k_a = 4\pi n_i / \lambda. \quad (2.33)$$

The real and imaginary parts of the index are not independent, but connected by integral relations. Given one set of indices over a sufficiently large band of frequencies, the other can be obtained by simple integration. For a derivation of these relations, please see Bohren and Huffman [1983], pp. 19-22. The Kramers-Kronig relations (also known as the dispersion relations) relate the real and imaginary parts of the complex index of refraction of a material, based on the assumptions of linearity

and causality in the interaction of a frequency dependent electric field with matter. We compute the real index of refraction of the dust particles at each wavenumber using information about the imaginary indices of refraction at all wavenumbers in the spectrum. The dispersion relations can be written in many different forms, and many different methods for solving the integral equations have been used [Warren, 1984].

The following subtractive-Kramers-Kronig (SKK) relation is chosen for our calculations since it is the preferred method if  $n_{im}$  is known only in a short spectral region [Warren, 1984, Ahrenkiel, 1971, Bachrach and Brown, 1970, Hale and Querry, 1973].

$$n_r(\lambda_0) = n_r(\lambda_1) + \frac{2(\lambda_1^2 - \lambda_0^2)}{\pi} P \int_0^\infty \frac{\lambda^2 n_{im}(\lambda)}{(\lambda_0^2 - \lambda^2)(\lambda_1^2 - \lambda^2)} d(\ln \lambda). \quad (2.34)$$

where  $P$  is the Cauchy Principle Value of the integral. The above can be rewritten as

$$n_r(\lambda_0) = n_r(\lambda_1) + \frac{2}{\pi} \int_0^\infty \lambda^2 n_{im}(\lambda) \left[ \frac{1}{(\lambda^2 - \lambda_1^2)} - \frac{1}{(\lambda^2 - \lambda_0^2)} \right] d(\ln \lambda). \quad (2.35)$$

In our model, we provide the Kramers-Kronig code with a limited range of imaginary indices of refraction (thermal infrared, 5-40  $\mu\text{m}$ ), and give it a known value of the real index at a wavelength in the visible region of the spectrum ( $\lambda_0 = 0.5 \mu\text{m}$ ), for which the properties have been well established [Ockert-Bell *et al.*, 1997].

We use a modified version of the code written by Sinnott at NASA Ames Research Center [Pollack, private communication]. The subroutine numerically integrates the integral in pieces on both sides of each singularity and sums them. It interpolates linearly if the wavelength is within the range for which data exist and extrapolates if not, according to the following:

$$\begin{aligned} n_i(\lambda) &\approx n_i(\lambda_{smallest}) \lambda^3 & \text{for } \lambda \leq \lambda_{smallest} \\ n_i(\lambda) &\approx n_i(\lambda_{largest}) \lambda^{-1} & \text{for } \lambda \geq \lambda_{largest} \end{aligned} \quad (2.36)$$

The subroutine takes as input an array of wavenumbers (in decreasing order), a

set of imaginary indices of refraction at the given wavenumbers, a value for the corresponding real index of refraction at one reference wavelength, the size of the wavelength array, and an integration resolution factor. It returns the array of real indices of refraction corresponding to the imaginary set it was given. Figure 2.2 shows the accuracy of the Kramers-Kronig subroutine. The bottom plot is the set of imaginary indices, and the top compares the actual real indices with the SKK computed ones (upper curve). The rms error between the calculated and actual indices is  $6.6 \times 10^{-2}$ . Removing the carbon dioxide band from the integration reduces the accuracy in the calculation, particular in wavenumber regions immediately adjacent to the  $15 \mu\text{m}$  band. The error caused by linear interpolation of this band in the calculations is shown.

Assuming the temperatures, optical depth, and particle size distribution to be known, there can exist at every wavelength more than one complex index of refraction which will generate a given brightness temperature. If there are two solutions, one represents the scattering solution and the other the absorbing solution. Although not every complex index is physically feasible, this non-uniqueness makes an inversion of the data problematic. The phase space is not well suited the type of search necessary to find one value for  $n_i$  which produces minimum error. A technique for simultaneously matching multiple orbital spectra to eliminate the ambiguity was developed [Toon, personal communication]. One unique set of imaginary and real indices of refraction can be found which generates brightness spectra that match multiple data sets simultaneously.

The same type of bracketed bisection search is used for the optical properties. The code can either search only on  $n_i$ , which can sometimes cause difficulties in non-absorbing regions where the brightness temperature is more sensitive to the real index than to the imaginary, or it can search on both  $n_i$  and  $n_r$  in parallel then combine them gradually to iteratively obtain a physically consistent set of properties.



Figure 2.2: Real indices of refraction for Montmorillonite 219b [Toon *et al.* 1977] calculated with Kramers Kronig by integrating over all wavenumbers ( $250\text{-}2000\text{ cm}^{-1}$ ) (dashed) and calculated without the  $\text{CO}_2$  band (dotted) compared with the actual values (solid).

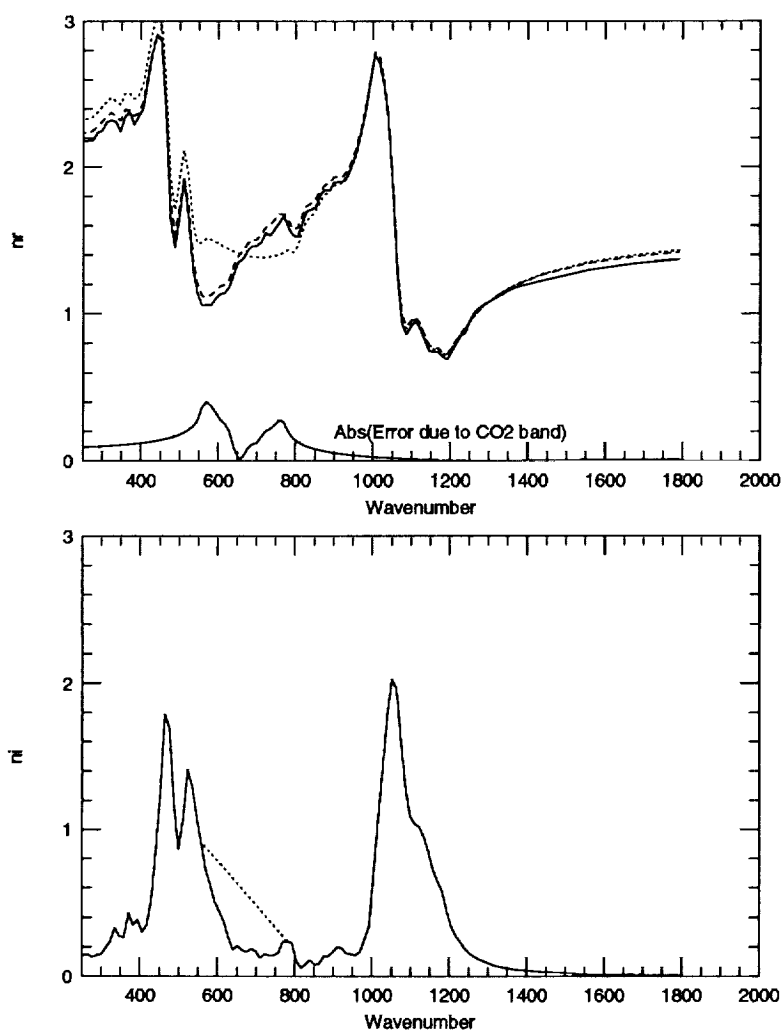
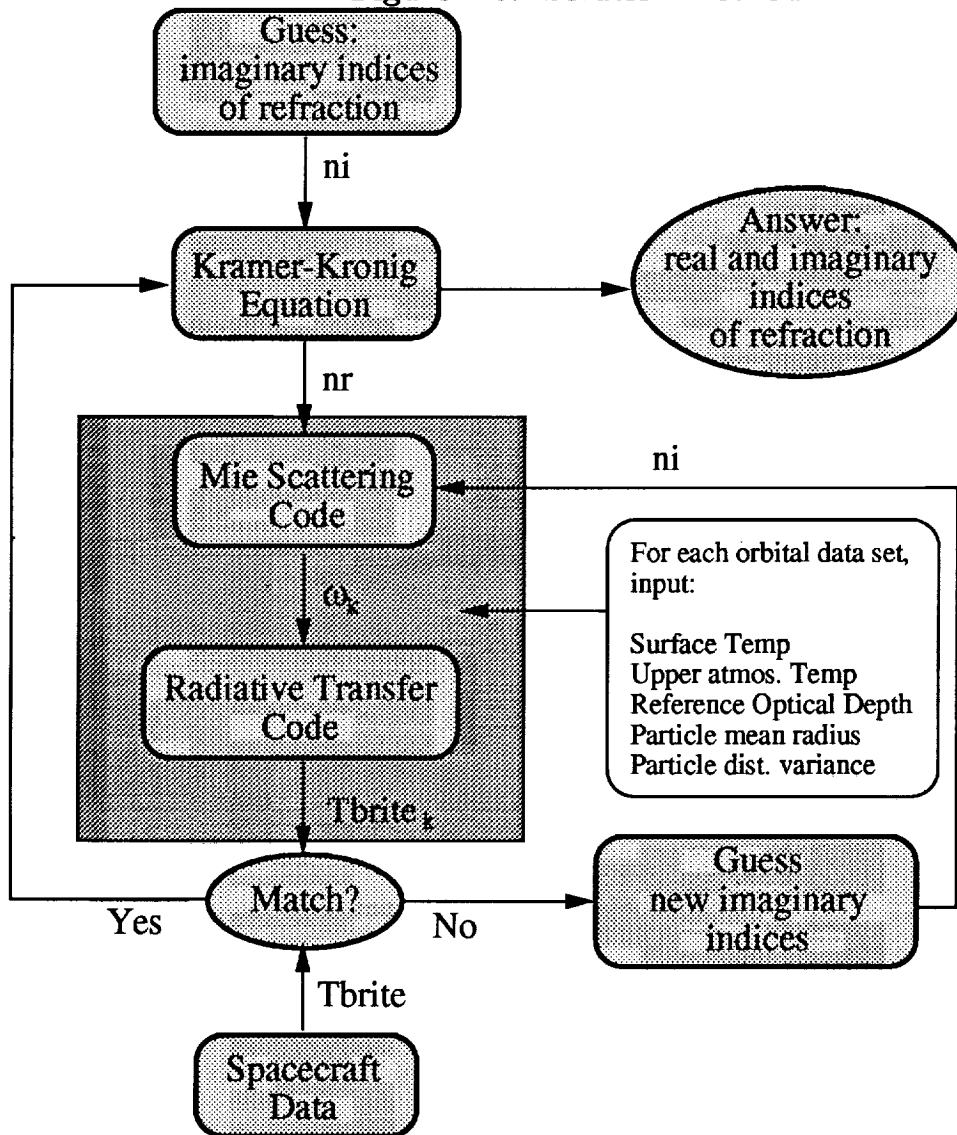


Figure 2.3: Solution method



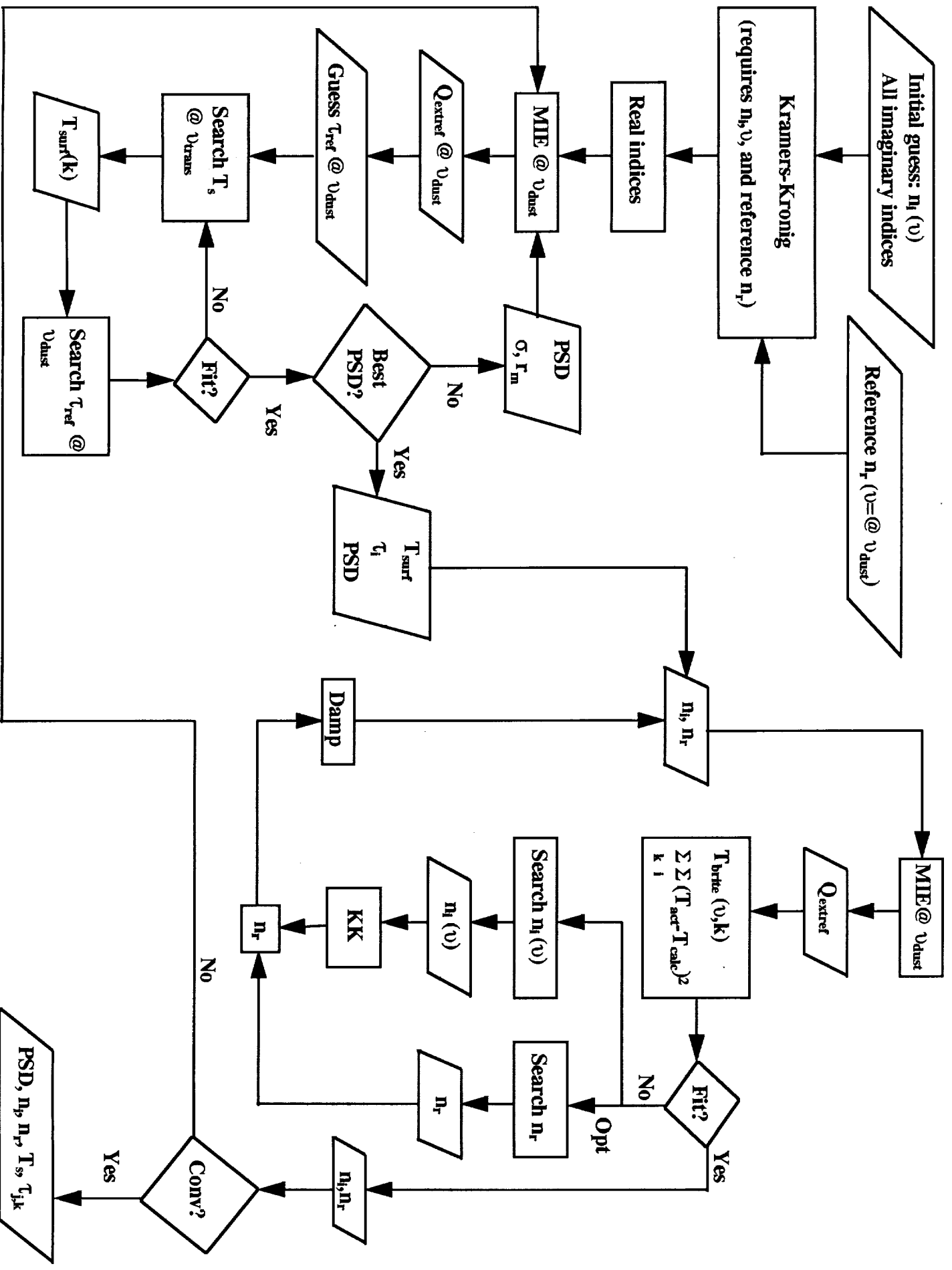
Convergence Parameter  $\chi_i = \sum_{k=1}^{10} (Tbrite_i|_{act} - Tbrite_i|_{calc})^2$

**Table 2.2: Test Parameters, (Ockert-Bell *et al.* [1997] particle size distribution)**

Optical Depth (reference) $\nu=1075\text{ cm}^{-1}$	View Angle $\cos \Theta$	Bottom Atm. Temp. (K)	Top Atm. Temp. (K)	Surface Temp. (K)	Mean particle radius $r_0\text{ }(\mu\text{m})$	Var( $\ln r_0$ )
1.286	0.417	214.177	243.746	266.000	0.660	0.642
1.417	0.904	199.792	259.488	260.000	0.660	0.642
1.024	0.969	196.730	258.875	263.000	0.660	0.642
0.761	0.387	191.079	246.290	278.000	0.660	0.642
0.442	0.996	179.595	249.974	275.000	0.660	0.642
0.424	0.982	178.460	255.760	278.000	0.660	0.642
0.405	0.527	174.716	245.766	281.000	0.660	0.642
0.349	0.505	168.652	241.217	278.000	0.660	0.642
0.349	0.980	168.652	241.217	278.000	0.660	0.642
0.235	0.974	169.684	240.538	281.000	0.660	0.642

## 2.4 Test Case

To demonstrate our techniques, we have constructed ten brightness temperature spectra using montmorillonite 219b, for which the optical properties are known, using different optical depths and surface temperatures, as shown in Table 2.2. These values were chosen in order to verify our model with previous work, and to test convergence of the various search techniques. The ten synthetic spectra generated using these parameters and montmorillonite 219b are treated as they were to be matched, then the searches on surface temperature, optical depth, and optical properties are carried out and the results compared to the known values. The search on particle size was not verified using this test case.



### 3. Results and Discussion

Given a reasonable initial guess for the indices of refraction, the searches converge in a well-behaved fashion, producing a fit with error of less than 1.2 Kelvin (rms) to the observed brightness spectra. The particle size distribution corresponding to the best fit was a lognormal distribution with a mean particle radius,  $r_m = 0.66$ , and variance,  $\sigma^2 = 0.412$  ( $r_{eff} = 1.85$ ,  $\nu_{eff} = .51$ ) (see Figure 3.7), in close agreement with the size distribution found to be the best fit in the visible wavelengths in recent studies by Pollack *et al.*, [1995] and Ockert-Bell *et al.* [1997]. Figure 3.1 shows the final fit for all spectra (solid line) to the data (points) for each orbital dataset, beginning with the earliest (dustiest) orbit 008 in the upper left and ending with the latest (clear) orbit 206 in the lower right corner. The optical properties which were found to best match the data are shown in the lower plot of Figures 3.2- 3.4, with the dashed lines representing the initial input to the search, and the solid lines representing the converged result. The orbital parameters which correspond to these optical properties and which were also found iteratively during this search are shown in Table 3.1 and in Figure 3.5 by solid lines. Resulting scattering properties and opacities for one of the dustier orbits are shown in Figure 3.6. Since we have assumed a spatially and temporally constant particle size distribution and composition, these values of single scattering albedo and asymmetry factor represent all orbits, but the opacities scale for each orbit according to the density of the dust at the particular time of measurement. Again, the values found by Toon *et al.* are shown for comparison.

#### 3.0.1 Uniqueness

The problem examined here is as follows: given a measurement or series of measurements of thermal radiation emitted by an atmosphere, the intensity and spectral distribution of which depend on the state of the atmosphere in a known way, deduce the best estimate of the properties of the atmosphere. There are two distinct aspects to this problem which are not always clearly separated; they may

Figure 3.1: Fit produced by the new optical properties shown in Figure 3.2 to brightness temperatures measured for orbits ranging from dusty ( $\tau(9\mu m) = 1.5$ ) (upper left) to clear ( $\tau = 0.18$ ). The observations are represented by points and the fits are solid lines.

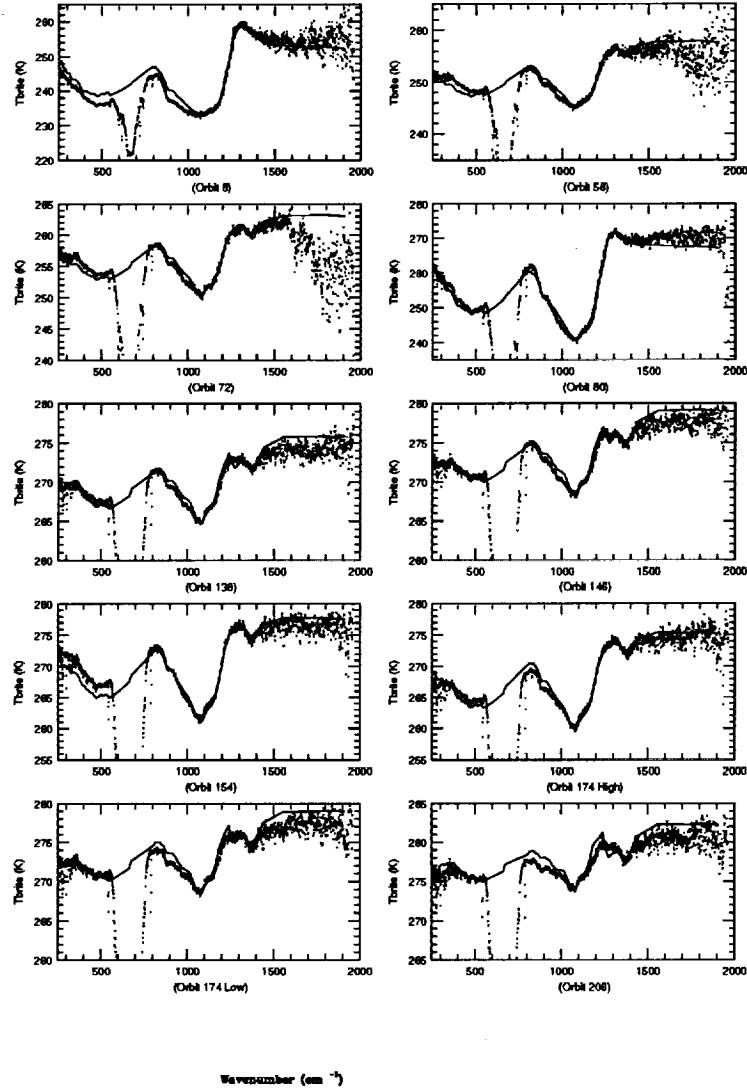


Figure 3.2: Upper plot shows initial (dashed line) and final fit (solid line) to the Mariner 9 spectra (points) for orbit 8. Lower plot gives the initial (dashed lines) and final (solid and dotted lines) optical properties which produced the temperatures in the upper plot.

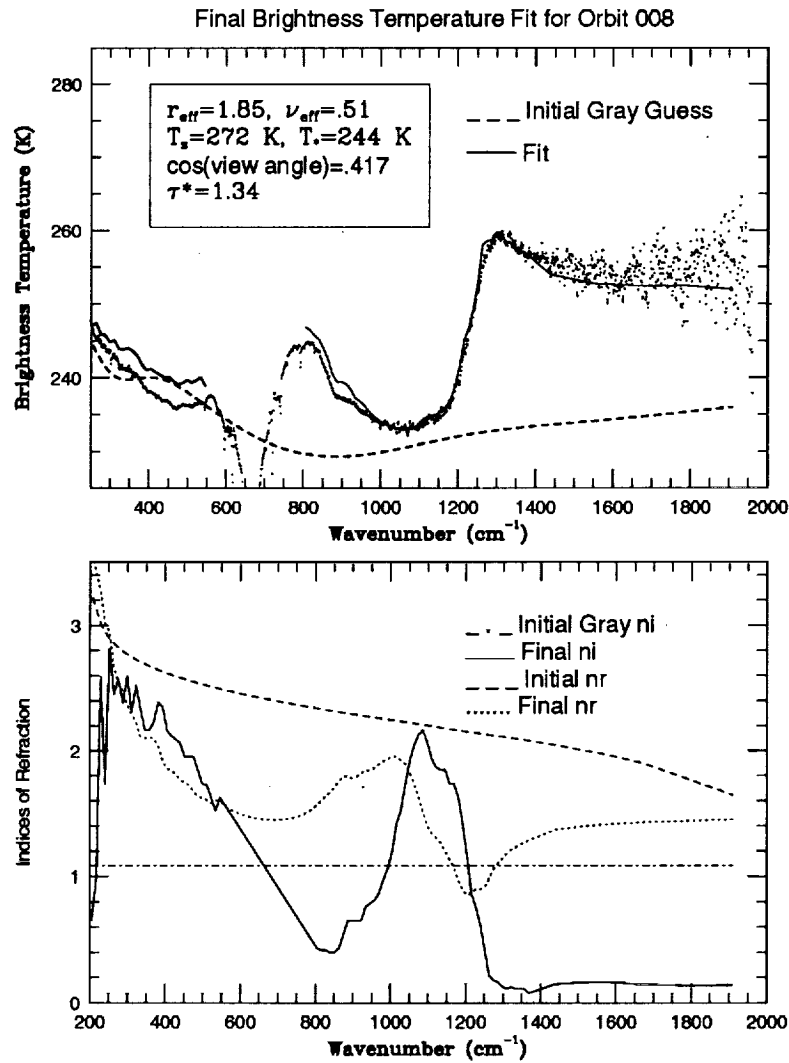


Figure 3.3: Upper plot shows initial (dashed line) and final fit (solid line) to the Mariner 9 spectra (points) for orbit 80. Lower plot gives the initial (dashed lines) and final (solid and dotted lines) optical properties which produced the temperatures in the upper plot.

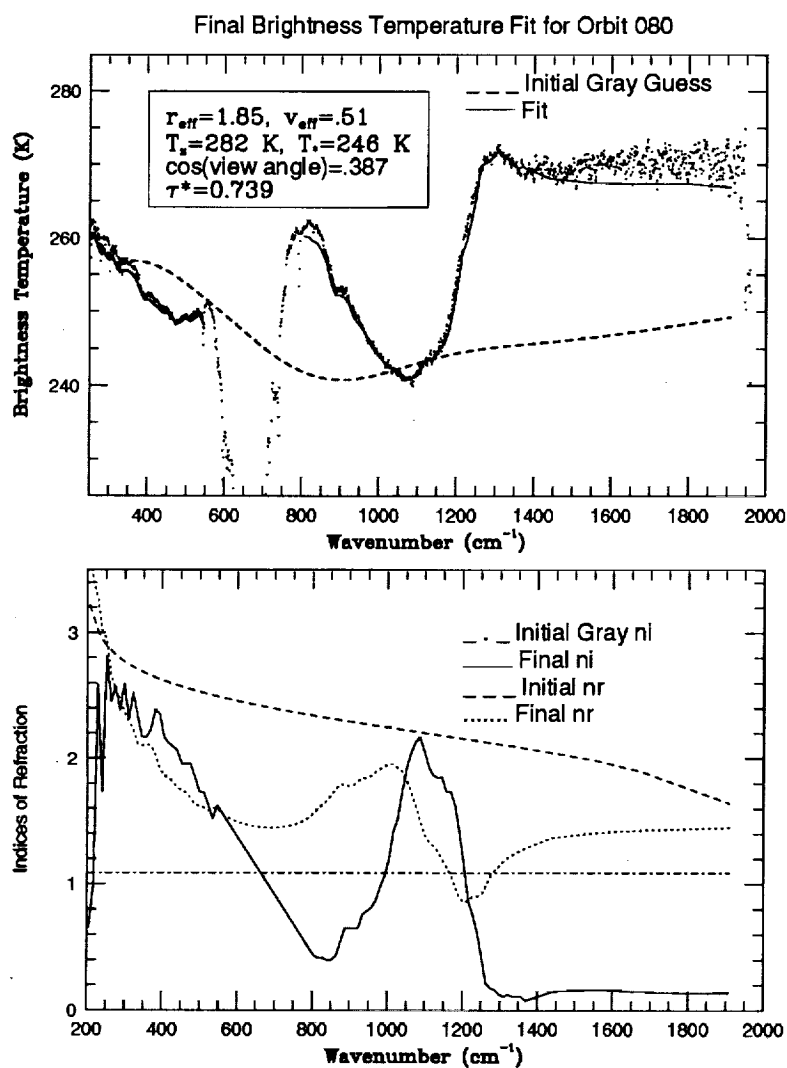




Figure 3.4: Upper plot shows initial (dashed line) and final fit (solid line) to the Mariner 9 spectra (points) for orbit 8. Lower plot gives the initial (dashed lines) and final (solid and dotted lines) optical properties which produced the temperatures in the upper plot.

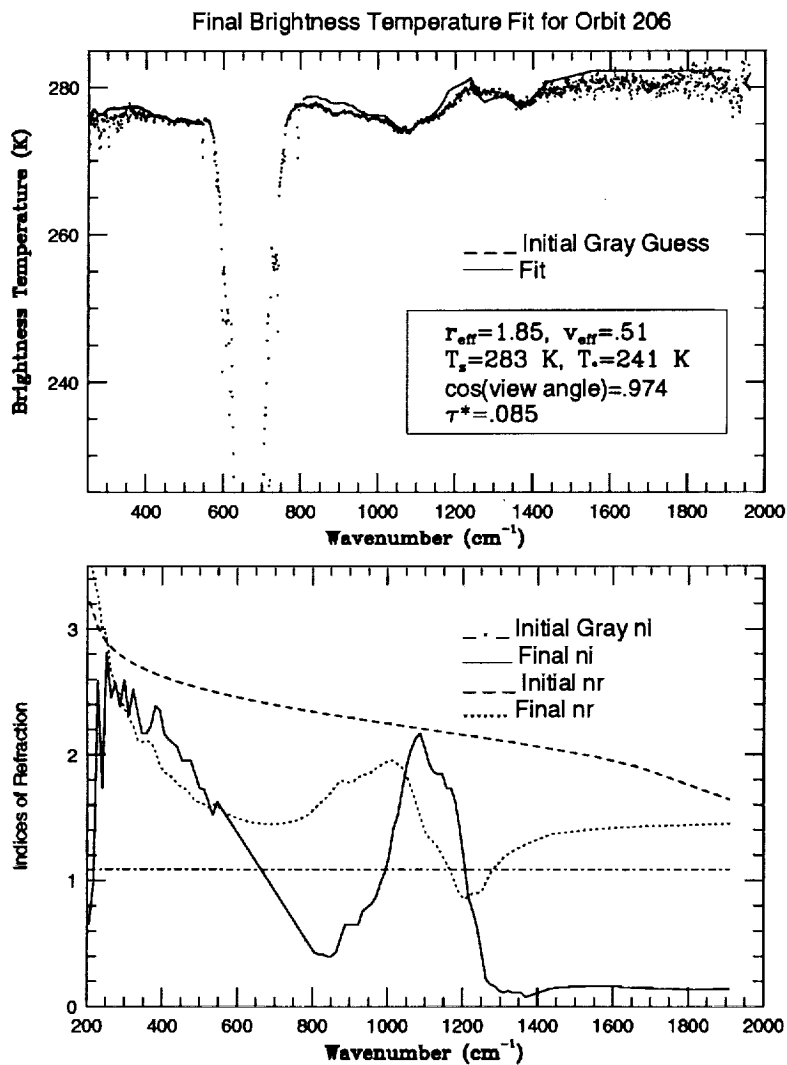


Figure 3.5: The solid lines in the upper plot show the surface temperature (higher solid line) and the atmospheric temperature near the surface (lower solid line) during the decay of the dust storm. For comparison, the assumption made by Toon *et al.* is illustrated by the dashed line, and a very crude verification of trends obtained from the LMD database [Forget *et al.* 1998] is given by the dotted lines. The lower plot compares the new inverted opacity at a wavelength of 9  $\mu\text{m}$  with the opacity assumed by Toon *et al.* , [1977].

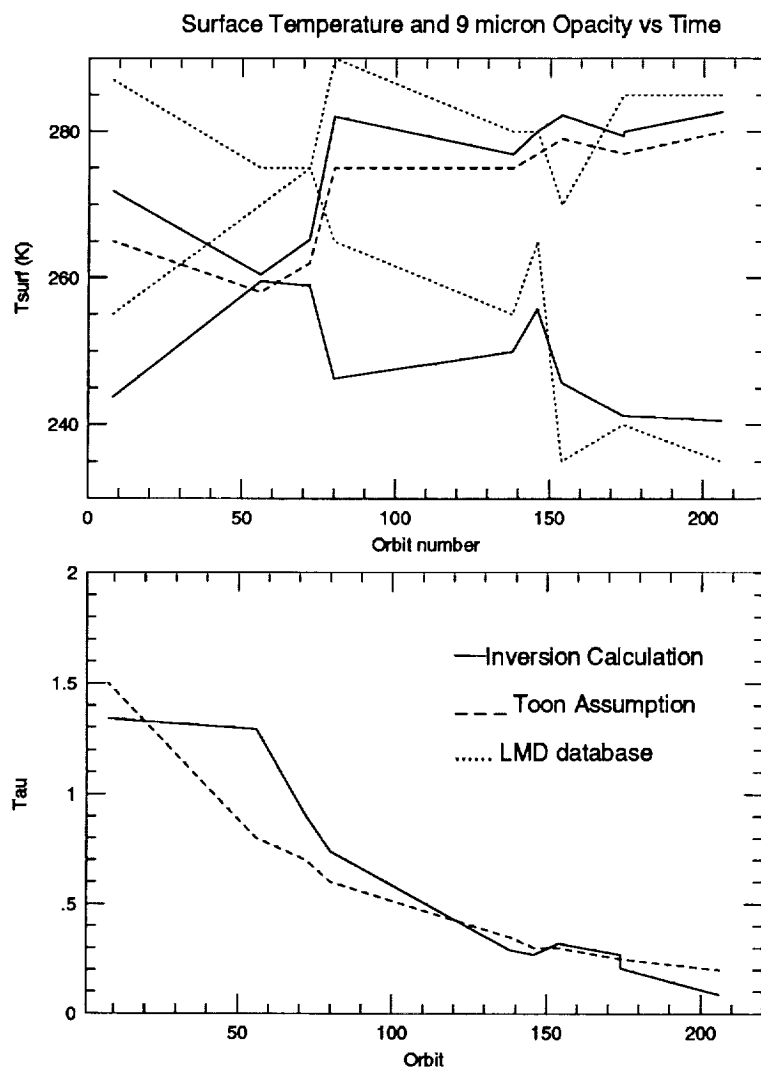
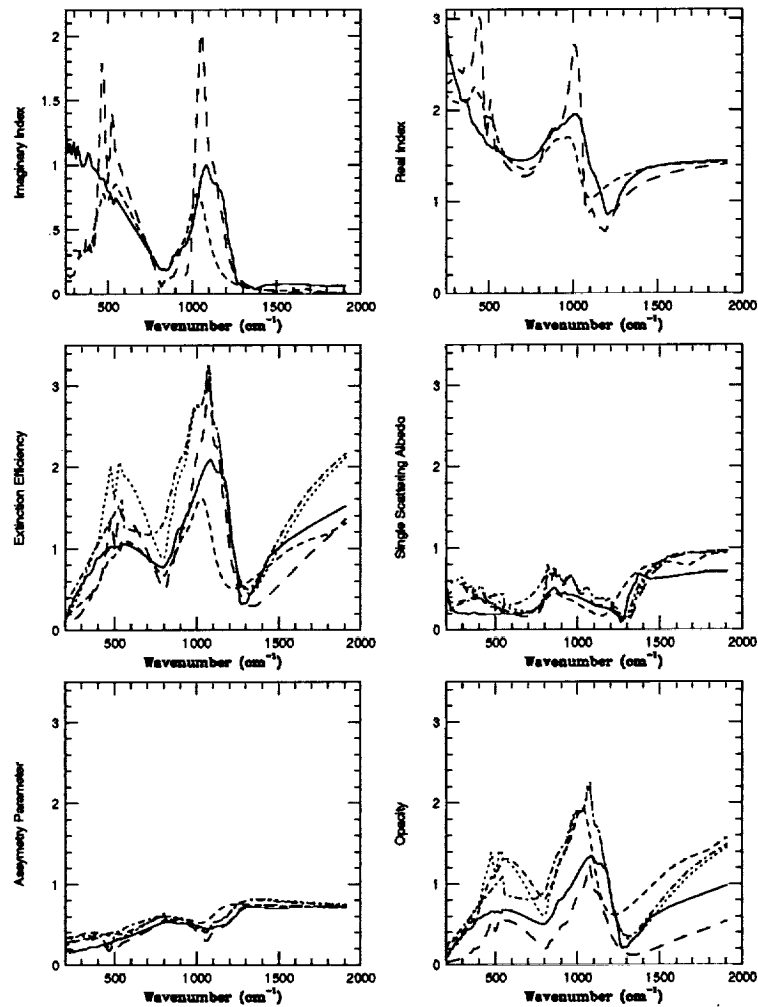


Figure 3.6: Final computed optical properties (top), with new properties shown by the solid lines, montmorillonite shown by the long dashes, and palagonite shown by the short dashes. Extinction efficiency,  $Q_{ext}$ , (middle left) single scattering albedo,  $\omega$ , (middle right) asymmetry parameter,  $g$ , (bottom left), and spectral opacity,  $\tau_\lambda$ , are compared for various studies.



Solid line: Snook, .... Toon, --- Clancy, -.- Pollack, \_ \_ \_ Forget

be described as the 'inverse' problem and the 'estimation' problem. The inverse problem is the matter of inverting a known equation which expresses radiation as a function of the atmospheric state, so as to express the atmospheric state in terms of radiation. This is usually an 'ill-posed' problem; i.e., it has no mathematically unique solution [Rodgers, 1972]. We therefore have an estimation problem, that is, to find the appropriate criteria which determine the best solution from all the possible ones which are consistent with the observations.

We have dealt with this situation of non-uniqueness in two ways. First, we have made approximations to the equations of radiative transfer by discretizing continuous functions of altitude, wavenumber, and view angle, or by expanding functions in Taylor series or Legendre polynomials. Secondly, we have imposed constraints on a large number of the unknowns based on strong physical arguments which will be discussed in Section 3.0.2.

Our resulting problem is one which consists of many more equations than unknowns, but the equations are very strongly coupled and non-orthogonal. Specifically, there exists an equation of radiative transfer which relates the our unknowns (the indices of refraction, the surface Temperatures, the particle size distribution, and the opacity) to the measured radiance quantity at each wavelength and for each orbit. There also exists at each wavelength one Kramers Kronig relation which relates the value of the real index of refraction of the material to the integral of the imaginary indices over all wavelengths. We have selected ten datasets of 85 wavelengths over which to solve these equations. Thus, we have  $10 \times 85 + 85 = 935$  total equations. Our remaining unknowns after discretization and physical constraints are 9 surface temperatures (one for each orbit), 9 reference optical depths, 85 imaginary indices of refraction, and 85 real indices of refraction, one mean particle radius, and one size distribution variance, for a total of  $9 + 9 + 85 + 1 + 1 = 105$  total unknowns.

Once the problem has been so reduced, we may treat it as well-posed in the immediate vicinity of the solution. We use the common technique of a least squares fit in the error between the computed and observed brightness temperatures. The 105-dimensional phase space over which we must search is riddled with local minima. We search on each parameter individually by traversing one dimension of the phase

space at a time and finding the minimum in each dimension. The dimensions of phase space for  $n_i$ ,  $n_r$ ,  $\tau$ , and  $T_s$ , are well behaved in the vicinity of the solution, with either one or two sharp minima which are easy to find. Provided we do not stray too far from the actual solution with our initial guess, the result of the iterative search scheme finds the appropriate solution. However, the scheme is not generally robust. That is to say, it is prone to either divergence or convergence to any number of mathematically feasible results, if given a bad initial set of parameters. This would not be a problem if all solutions besides the right one were physically unrealistic and could be ruled out on the basis of physical arguments. However, we have found that many physically feasible solutions exist.

Fortunately, we know enough about the physics of the situation to ensure that we start with a guess which is close enough to the solution to avoid the above mentioned problems of divergence or wrong results. In addition, our data are noisy and are averaged over many measurements, which tends to damp out minima in the actual phase space, making the search more robust than it otherwise would be.

To investigate the robustness of the search, we constructed a test case by using a known spectrum of optical properties to calculate brightness temperatures for various values of optical depth and surface/atmospheric temperatures and then attempted to invert the problem to obtain the values we started with. This artificial test case had an unfriendly phase space with sharp multiple minima which would trap the search in incorrect solutions and which even diverged from the correct solution if perturbed slightly. There seemed to be a finite number of incorrect solutions for the limited number of initial guesses we tried. That is, most initial guesses converged to one of three or general solutions.

We then added noise to the test case and discovered that this greatly reduced the undesirable behavior of the search, and the model was capable of converging to the right answer given any reasonable initial guess. In fact, with noise comparable to that found in the actual data, it was possible to start with a flat gray guess for the imaginary indices of refraction (a very bad guess, indeed) and obtain the correct solution.

Thus we are confident that while the solution we have obtained is not unique,

it is the correct one, since we know we are starting with an initial guess which is within the tolerance of proximity to the actual solution. Figures 3.2-3.4 show in dotted lines our initial gray guess, and the final converged answer for the optical properties, along with the fits to the brightness temperature spectra. This solution is the one obtained by a large number of initial guesses, increasing our degree of certainty in the result.

### 3.0.2 Accuracy of the model and plausibility of the results

Now that we are confident in the results of the code used to invert the spectra, we must convince ourselves that the assumptions made in order to solve the equations on which the code is based and the results which the code generates are justifiable and physically realistic.

#### 3.0.2.1 Particle Size distribution

Of all the free parameters in this problem, the particle size distribution has proven to be the most difficult to invert directly. The minimum in the particle size distribution phase space is very broad and covers a large range of radii. We had originally intended to consider the particle size distribution parameters as totally free, and to try to invert them directly with the rest of the free parameters. However, limitations on the computational time combined with the large number of possible solutions in this dimension of phase space led us to conclude that this aspect of the problem was better suited to individual case studies rather than a sweeping broad search of all possible particle size distributions.

For our case studies, we focused attention on particle size distributions which have been proposed in the literature [Hanel *et al.* , 1972, Hunt *et al.* , 1972, Conrath *et al.* , 1973, Toon *et al.* , 1977, Santee *et al.* 1993, Clancy *et al.* , 1995, Pollack *et al.* 1995, Forget *et al.* 1997, Ockert-Bell *et al.* 1997]. Some of the distributions which produced the best fit in our model are shown in Figure 3.7. We used single-mode lognormal distributions with equivalent effective radius and variances (see Chapter 2 to the previously proposed modified gamma distributions. Hansen and Travis [1974] demonstrated that the effective radius and effective variance are the only important parameters of the size distribution, and that the radiative transfer equation is not

sensitive to differences between types of distributions (eg. the differences between lognormal and modified gamma type distributions) in the infrared wavelengths.

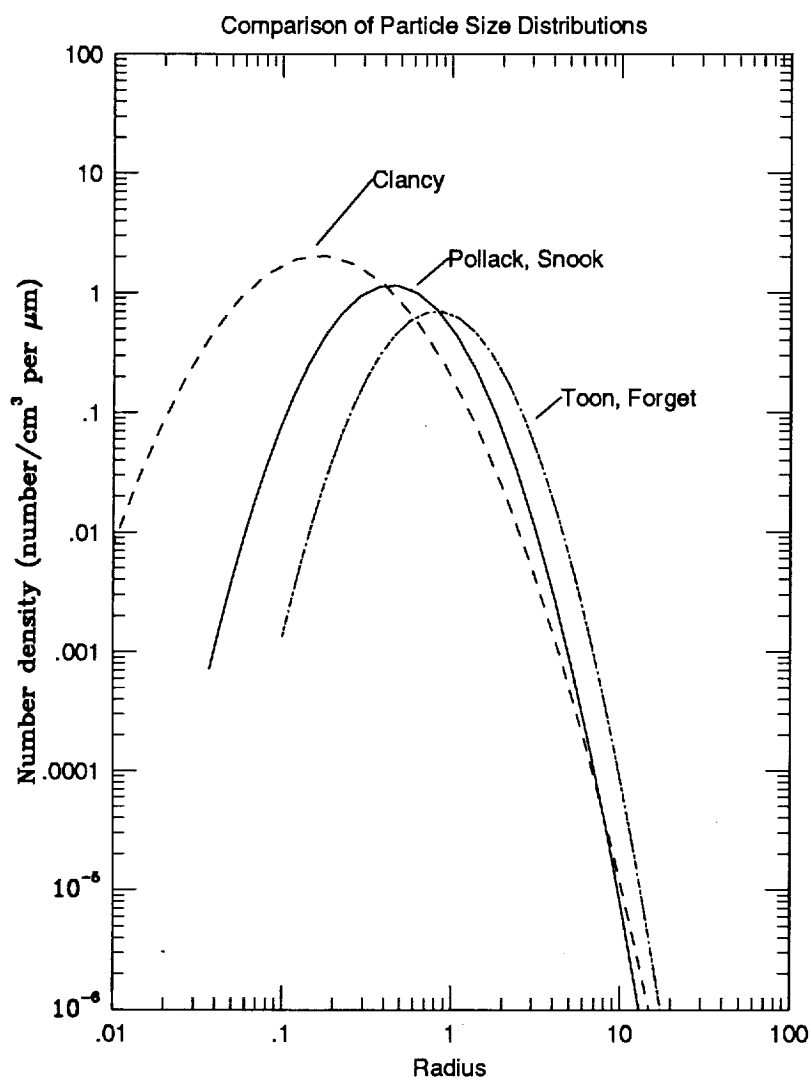
All size distributions which were investigated represent physically plausible particles, although those proposed by Clancy *et al.* [1995] are probably too small, and those proposed by Toon *et al.* [1977] are probably too big. Multi-modal size distributions (representing mixtures of very different materials) were not considered.

The particle size distribution which was ultimately chosen as the best was  $\tau_{eff} = 1.85$ ,  $\nu_{eff} = .51$ , also found by Ockert-Bell *et al.* [1997] and Pollack *et al.* [1995] to provide the best fit to spectra at visible wavelengths. Previous attempts to fit brightness temperature spectra of earth analog materials using this size distribution had failed to produce a suitable result in the infrared [Clancy *et al.* 1995], but we find it is possible to fit all brightness temperature spectra using our inverted optical properties and this particle size distribution. Thus, we now have a proposed size distribution which can fit data from the infrared to the ultraviolet extremes of the spectrum. This continuity of fit over all regions of the spectrum is a strong argument in favor of this particular distribution.

Numerical integration over particle size in the calculation of the Mie scattering parameters introduces only a small error in the calculations, since an accurate gaussian quadrature is used to determine weights and abscissas for the integration, and a high number of intervals is used

Two other important assumptions regarding the particle size distribution were made in this analysis: 1) particles were uniformly mixed throughout the atmosphere and 2) particle size distribution remained constant throughout the duration of the storm. The first assumption is probably an accurate one, based on calculations of wind speeds and eddy velocities [Toon *et al.* 1977, Haberle *et al.* 1996], showing that winds are strong enough to keep the dust well mixed up to altitudes of 50 km. Our results suggest that second assumption, however, may not be so accurate. Figure 3.1 clearly shows an overprediction of brightness temperature on orbit 8 over the region of the spectrum most sensitive to particle size ( $450 \text{ cm}^{-1}$ ), and an underprediction later in the storm on orbit 154, indicating that the particles might actually be bigger than assumed near the beginning of the storm and smaller than assumed towards

Figure 3.7: Lognormal particle size distributions with effective radii and effective variance corresponding to distributions used by Toon *et al.* [1977], Pollack *et al.* [1995], Clancy *et al.* [1995], Forget *et al.* [1997], and author].





the later clearing stages. Nevertheless, the fits are still the best ever found in this region of the spectrum (see Section 3.0.4), and will only improve once variation in particle size with time is taken into consideration.

### 3.0.2.2 Optical Properties

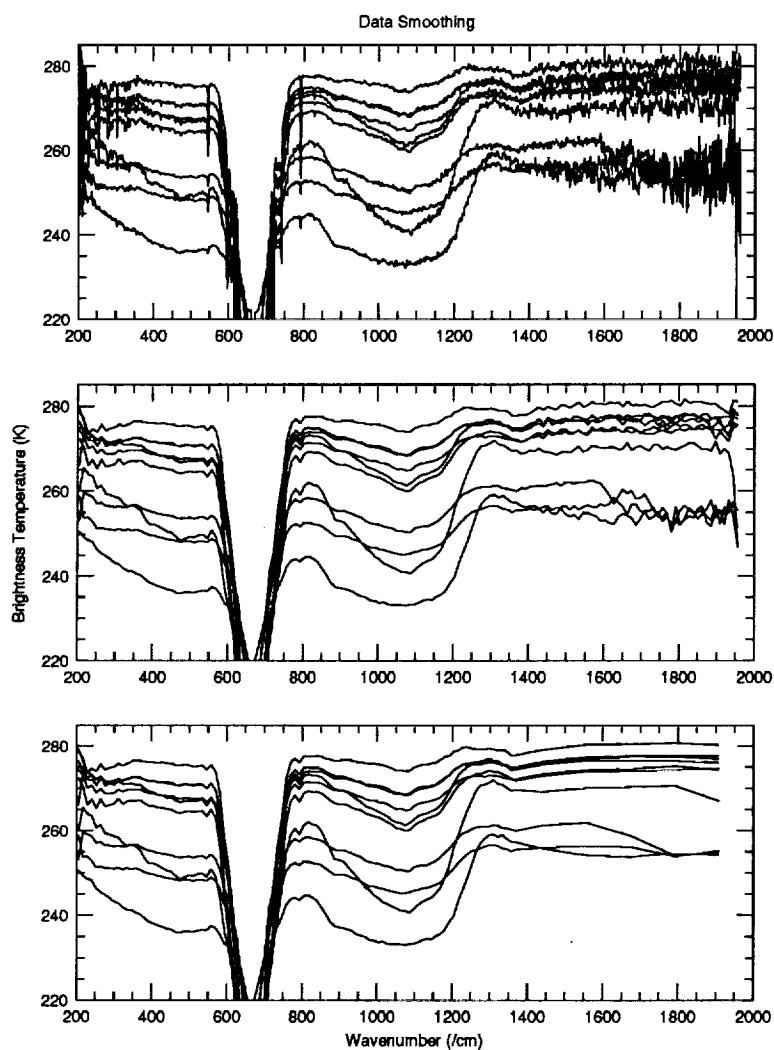
The only *a priori* assumption made regarding the optical properties is that the composition of the dust remains constant. That is, the density of the dust may change throughout the storm, but the dust has the same intrinsic material properties at the beginning of the storm as at the end. The data Figure 3.8 support this assumption, since the absorption and transmission features for all spectra occur at identical wavelengths, and all spectra are self-similar to first order.

It is difficult to say how well the Kramers Kronig equations represent the actual correlation between the real and imaginary indices of refraction, since most measurements of optical properties in laboratories employ various theories, including Kramers Kronig, to obtain self-consistent real and imaginary indices of refraction. For example, all "actual" material properties employ Kramers Kronig relations, Habke theory, or dispersion analysis in some form [Rousch, 1994]. The Kramers Kronig equations are exact, derived from the Maxwell equations, so they represent the best known relationship between the real and imaginary refractive indices. Again, the numerical integration of the relations introduces error near the region of the interpolated CO<sub>2</sub> band and near the endpoints of the region of integration, but the use of the subtractive forms of the relations reduces the effects of the truncation to the immediate vicinity of the endpoints. This has been discussed in greater detail in earlier sections and illustrated in Figure 2.2.

During the iteration procedures, there are moments when the real and imaginary indices of refraction are not Kramers Kronig consistent, but as the searches converge, this is no longer the case, and the resulting optical properties conform to the physical constraints imposed by the dispersion relations.

The optical properties which result from the iteration scheme have already been shown in Figure 3.2. Figure 3.6 demonstrates by comparison (top left and right) to properties of the analog materials, montmorillonite and palagonite, that the

**Figure 3.8:** This figure shows the similarity of the Mariner 9 datasets chosen for this analysis. In general, all 20,000 Mariner 9 spectra exhibit roughly the same behavior as shown here. The three plots show the successive smoothing employed, and also demonstrate the consistency of composition and material properties of the dust over time.



resulting indices of refraction realistic and exhibit the general absorption features expected in the region centered at approximately  $1075\text{ cm}^{-1}$  and  $550\text{ cm}^{-1}$  typical of silicate materials such as clays and basaltic weathering products. The problematic  $550\text{ cm}^{-1}$  double absorption peaks of the montmorillonite 219b imaginary index do not appear in our results. In addition, new absorption features appear in the small wavenumbers ( $< 500\text{ cm}^{-1}$ ) which have never been included in traditional silicate models of optical properties in the infrared. These features could be indicative of carbonates such as gypsum or calcite, which have similar properties at these wavelengths [Rousch, private communication, Long *et al.* 1993]. Gypsum and calcite have been identified by Viking and Pathfinder to be possible components in the Mars surface soils and rocks, so it would not be surprising to find some evidence of these minerals in atmospheric dust spectra. It is somewhat surprising that the absorption does not decrease near the limit of small wavenumbers. This could be due in part to the high level of noise in the data at these wavenumbers and in part to possible inaccuracies in particle size and shape. Near this Rayleigh scattering limit, the assumptions of spherical particles begin to become less accurate [Pollack, 1982].

The real index of refraction behaves as expected, with a phase-like response to the imaginary peak and asymptoting to the known value for  $n_r$  toward the visible end of the spectrum of 1.52 [Ockert-Bell, 1997].

### 3.0.2.3 Surface and Atmospheric Temperatures

The surface temperatures on which the model converges are within 8 K of the approximate surface temperatures given by the brightness temperature at the maximum point ( $1321\text{ cm}^{-1}$ ). The dashed line in Figure 3.5 shows the brightness temperature at the wavenumber for which the measured radiance is maximum, corresponding to the wavenumber of minimum opacity of the dust. Toon *et al.* [1977] assumed this value to be the temperature of the surface, and if we assume that the atmosphere is cooler than the surface, this dashed line represents the coldest possible surface temperature. We have not assumed that the dust is entirely transparent at any wavenumber, so the surface temperatures in our results (upper solid line in upper plot) are warmer than those assumed by Toon *et al.* . The lower solid line is

the value of the bottom temperature at the bottom of the atmosphere, just above the surface. Large temperature gradients between the surface and in the first few meters of the atmosphere have been observed by both Viking and Pathfinder, and we see this reflected in our results, particularly in the later clearer conditions, where the atmosphere above the surface is 40 Kelvin cooler than the surface itself.

An additional check of the physical reality of the temperatures at the time and place of each measurement was performed using the European Mars Climate Database at <http://www.lmd.jussieu.fr/mars.html> [Forget *et al.*, 1998]. This database combines data from Mariner 9, Phobos, Viking, and Pathfinder, and uses theoretical models for interpretation between datasets. The data are sparse and the models are coarse, but we obtained some rough verification of the trends in temperatures based on the database values for a dusty atmosphere ( $\tau = 2$ ) during the northern winter season. The dotted lines in the upper plot of Figure 3.5 show the values returned from the database, using a constant value 2 for the opacity until orbit 154 and abruptly switching to the “low dust” scenario after orbit 154. Clearly, this will return incorrect temperatures, since the opacity decreases smoothly from 1.5 to .2 over the course of the storm. Nevertheless, the relative values of the temperatures show the effects of time of day and location of measurement, and the slopes of the lines, particularly in the dustier orbits, closely match our results.

As discussed in Chapter 2, we do not consider the vertical temperature profile to be a free parameter. We use the temperatures inverted from the  $667\text{ cm}^{-1}$   $\text{CO}_2$  band by Pollack *et al.* [private communication], which do not take into consideration scattering or absorption by atmospheric dust. Other researchers [Santee and Crisp, 1993, Lindner, 1993] have attempted to treat the dust and  $\text{CO}_2$  simultaneously, but did not invert the particular spectra which we selected for our studies, and a detailed analysis of the combined  $\text{CO}_2$ /dust absorption is beyond the scope of this thesis. We therefore accept the error associated with the inverted temperatures, which is on the order of 5-10 Kelvin [Santee and Crisp, 1993]. Sensitivity studies involving these assumptions and errors are presented in Section 3.0.3. Since the radiative transfer equations are only very loosely coupled in wavelength, we are able to focus our attention on only those wavelengths outside the  $\text{CO}_2$  band, and we make no

claims regarding the optical properties in that band. We treat that region as one in which there is no data, which we can do because the radiative transfer equations are essentially monochromatic, and the Kramers Kronig equations are not sensitive to wavelengths far away from the one being calculated.

#### 3.0.2.4 Opacities

The opacity of the dust is considered to be a completely free parameter, with no *a priori* assumptions. The optical depth at wavenumber  $1075\text{ cm}^{-1}$  was iteratively determined for each orbit, and then opacities at all other wavelengths were computed using the extinction efficiency scaling ratio as discussed in Chapter 2.

The bottom plot of Figure 3.5 gives a normalized comparison of optical depth decay rate with that assumed by Toon *et al.* [1977]. The solid line is the result of our calculations, as compared with the dotted line which has been assumed in most studies of the Mariner 9 data. These assumptions were based on knowledge of opacities in other parts of the spectrum (eg. Viking opacity measurements in the visible during 2 dust storms) and on data from other instruments aboard Mariner 9. The trend in our results is clearly similar, but indicates that the dust probably persisted longer near the beginning of the storm until after orbit 60 when it began to decay.

#### 3.0.2.5 Other assumptions

We have included the effects of a spectrally varying surface emissivity, to reflect the conclusions of Christensen *et al.* [1998] that the surface signatures are included in the observations of radiance and must be separated from atmospheric effects. This represents the physical situation better than assuming the surface to be a black or gray body, such as Toon, Pollack, Forget, and Clancy have assumed, but is only an approximation based on the spectra measured during clear atmospheric conditions late in the Mariner 9 mission.

The multilayer radiative transfer model was verified using simple tests for which results were known.

### 3.0.3 Precision of calculations

Brightness temperature fits for all ten orbits are shown in Figure 3.2 - Figure 3.4. We find that the RMS error in brightness temperature is at or below the noise-equivalent  $\Delta T$  for all orbits. We have done a systematic set of studies to determine the sensitivity of our model to the various parameters listed in Table 2.1. Table 3.2 shows the rms error for our baseline result (Table 2.1), with a breakdown of error for each orbit. Each parameter was increased and decreased by 10%, except in the case of the Temperatures, which were increased and decreased by 5 K. All other parameters were held constant in all cases. We see that the rms error increases in all cases as we move away from our baseline answer, indicating that we have indeed found the best fit of these parameters for this given particle size distribution ( $r_{\text{eff}} = 1.85$ ,  $v_{\text{eff}} = 0.51$ , and giving an idea of the error bars for the results.

### 3.0.4 Implications of the results

There are two general categories of studies for which improved optical properties are necessary. First, current spacecraft measurements from orbit must be able to remove atmospheric effects in order to study the spectral properties of the surface. Current spectral models for the properties of the atmospheric dust in the infrared are inaccurate, as we will demonstrate. The atmosphere is always dusty, and therefore there will always be a need for accurate characterization of the spectral properties of the dust. Secondly, any measurements involving heating rate calculations of the surface or atmosphere require information about the radiative cooling properties of the suspended dust. These types of calculations are used in general climate models for Mars as well as science and engineering calculations for surface system thermal design and scientific measurements on the ground. The optical properties of the dust in the infrared are extremely important in any equation of radiative equilibrium on Mars, since dust is the only major source of opacity besides  $\text{CO}_2$  in the infrared, and the  $\text{CO}_2$  is mostly limited to a small portion of the infrared spectrum.

Figure 3.9 clearly represents the improvement in fit of our model over those of previous studies [Toon *et al.* , 1977, Pollack *et al.* , 1995, Clancy *et al.* , 1995, Forget *et al.* , 1997]. The quantity plotted is the square of the error between the

calculated and actual brightness temperatures, using the optical properties, particle size distributions, temperatures, and opacities as specified by each study. The particle size distributions assumed in each case are shown in Figure 3.7 and the values for some of the other free parameters used in the studies are shown in Table 3.3.

Toon *et al.* [1977] concluded that montmorillonite 219b, while it was the best fit of the materials tested in the study, could not be the only material in the Mars dust, because it was too absorbing in the  $500\text{ cm}^{-1}$  region. The fits to our selected spectra using montmorillonite 219b and using the particle size distribution assumed by Toon *et al.* ( $r_{eff} = 2.75, \nu_{eff} = .4182$ ) are shown in Figure 3.10. Note the severe discrepancies caused by the  $500\text{ cm}^{-1}$  absorption of montmorillonite.

Pollack *et al.* [1995] sought to obtain a particle size distribution which could fit observations in the visible while at the same time still fit the infrared. Using the same montmorillonite 219 optical properties, but a new particle smaller size distribution ( $r_{eff} = 2.75, \nu_{eff} = .4182$ ) produces the fits shown in Figure 3.11.

Clancy *et al.* [1995] proposed still smaller particles and proposed the material palagonite [Roush, 1994] as the analog for the optical properties. He found that the fit in the  $500\text{ cm}^{-1}$  region was much better than Toon and Pollack, but that the fit to the major  $1075\text{ cm}^{-1}$  feature was degraded. Brightness temperature using these assumptions are given in Figure 3.12.

Finally, Forget *et al.* [1997] empirically modified the optical properties of montmorillonite by setting  $n_i = \text{constant} = .5$  and  $n_r = \text{constant} = 2.2$  in the whole region from  $200\text{--}550\text{ cm}^{-1}$ . These optical properties produce a better fit in that wavenumber region, but they are not physically consistent with the Kramers Kronig relations. Fits produced using his optical properties are shown in Figure 3.13

Comparing our fits (see Figure 3.1) with all of the above demonstrates the spectral improvement in the fit to the data using the iterated optical properties, surface temperatures, and opacities, and using the particle size distribution of Pollack *et al.* .

The second category of calculations for which improved optical constants are necessary involve atmospheric heating rate or flux calculations. These quantities are hemispherical mean quantities, so it is not immediately obvious what the effect

**Figure 3.9:** This figure clearly illustrates the improvement in fit to the Mariner 9 brightness temperature spectra by comparing results calculated using indices of refraction and particle size distributions from various previous studies. Here we plot the square of the error between calculated and actual brightness temperatures at each wavelength. The total error integrated over the spectrum is given by Chi and is indicated for each study.

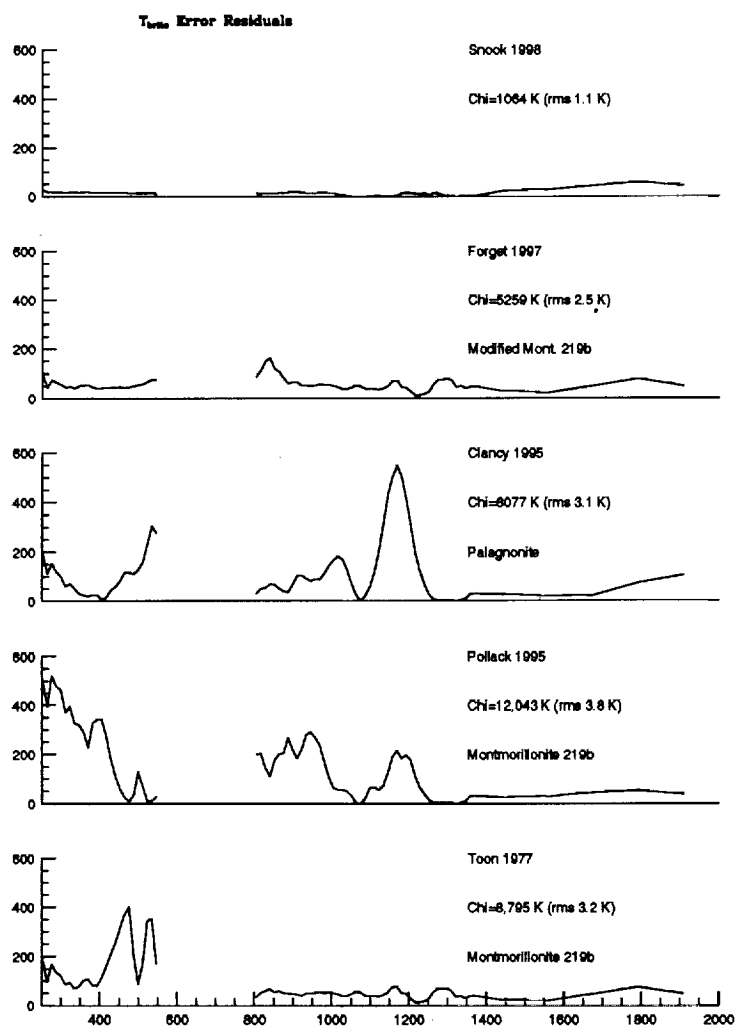
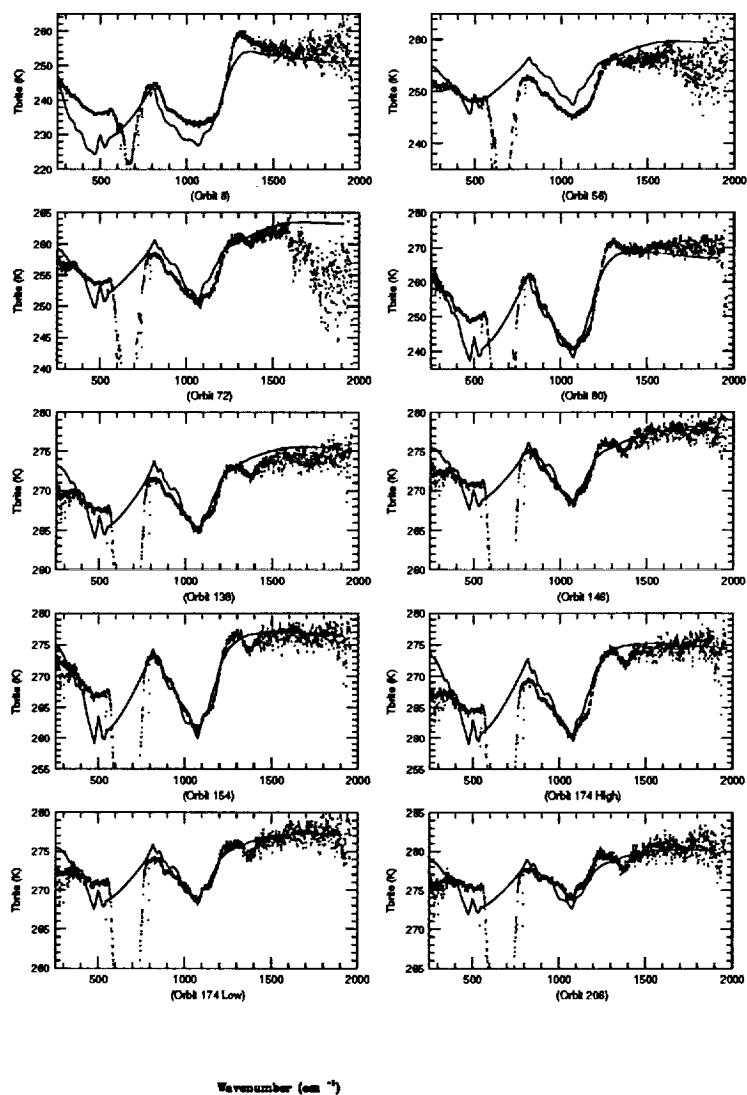




Figure 3.10: Fits to the selected brightness temperature spectra generated using the particle size distribution, optical properties, and temperatures assumed by Toon *et al.* [1977].



**Figure 3.11:** Fits to the selected brightness temperature spectra generated using the particle size distribution, optical properties, and temperatures assumed by Pollack *et al.* [1995].

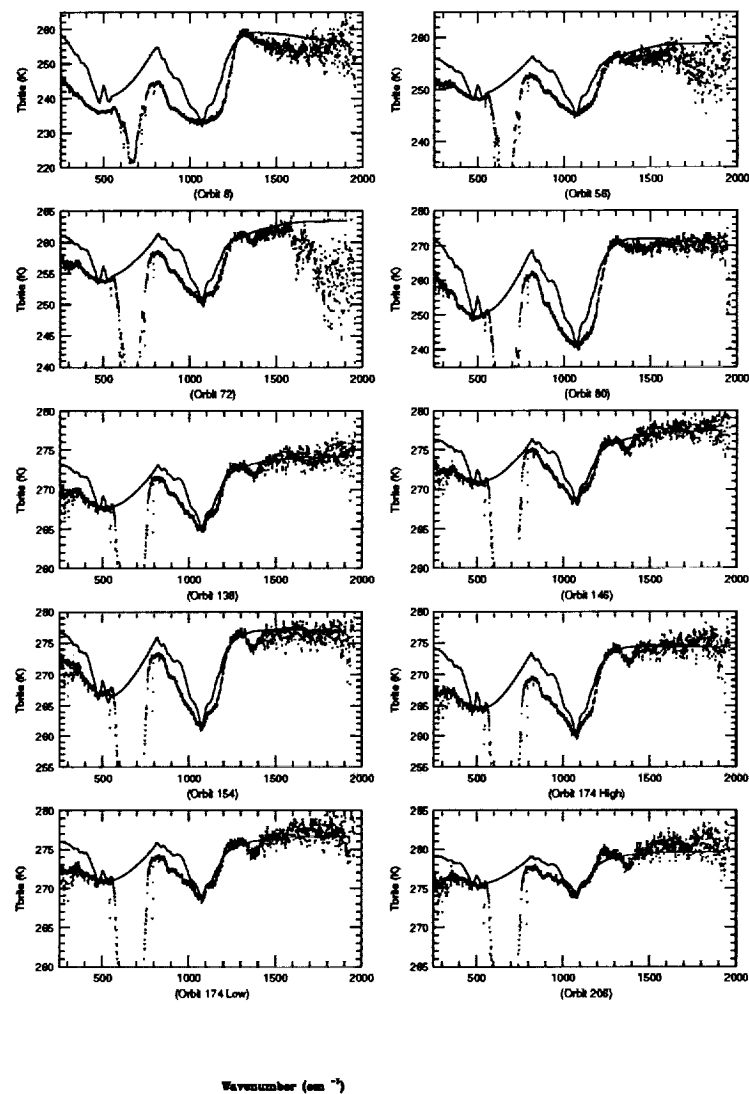


Figure 3.12: Fits to the selected brightness temperature spectra generated using the particle size distribution, optical properties, and temperatures assumed by Clancy *et al.* [1995].

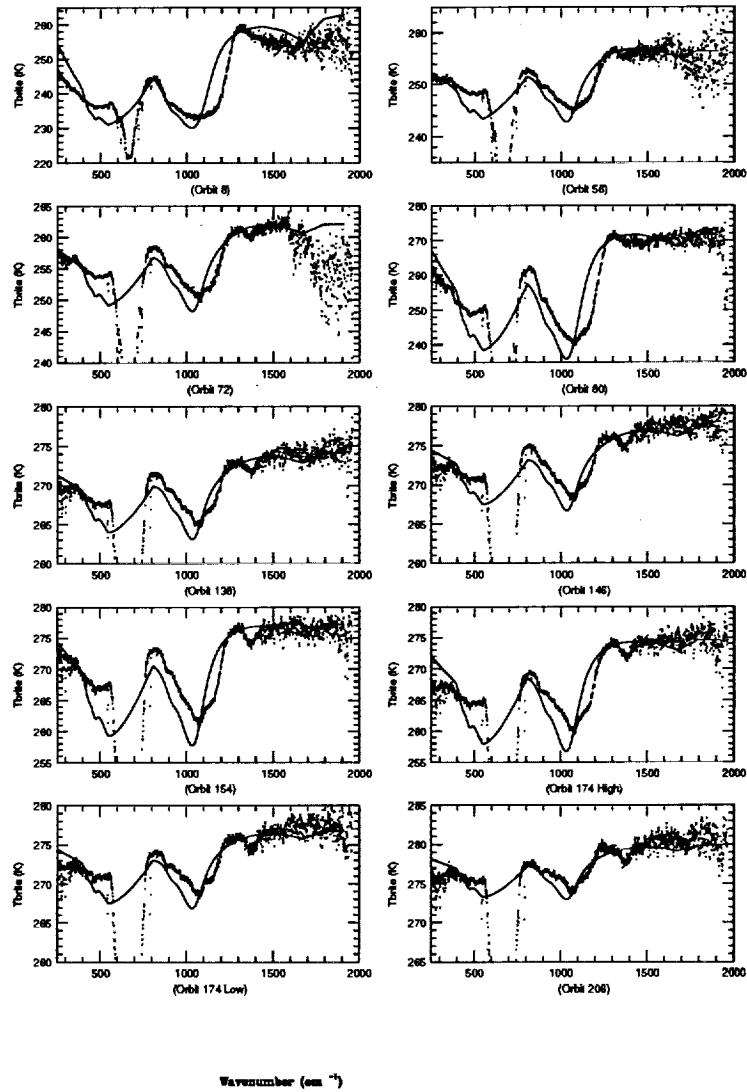
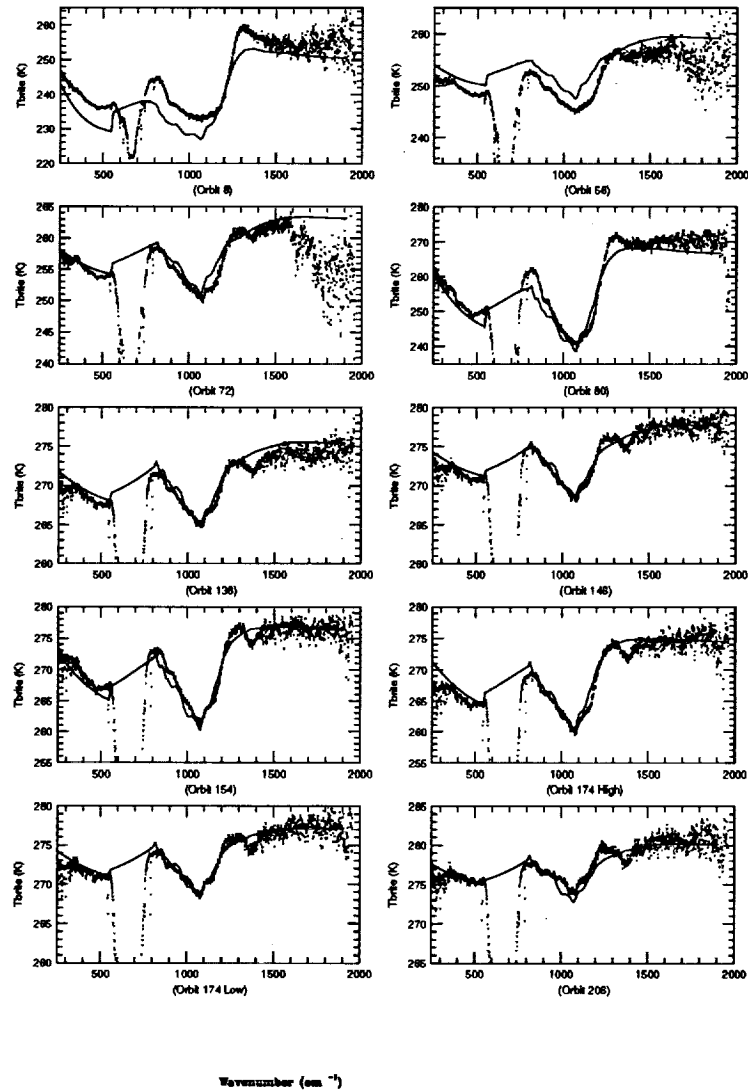
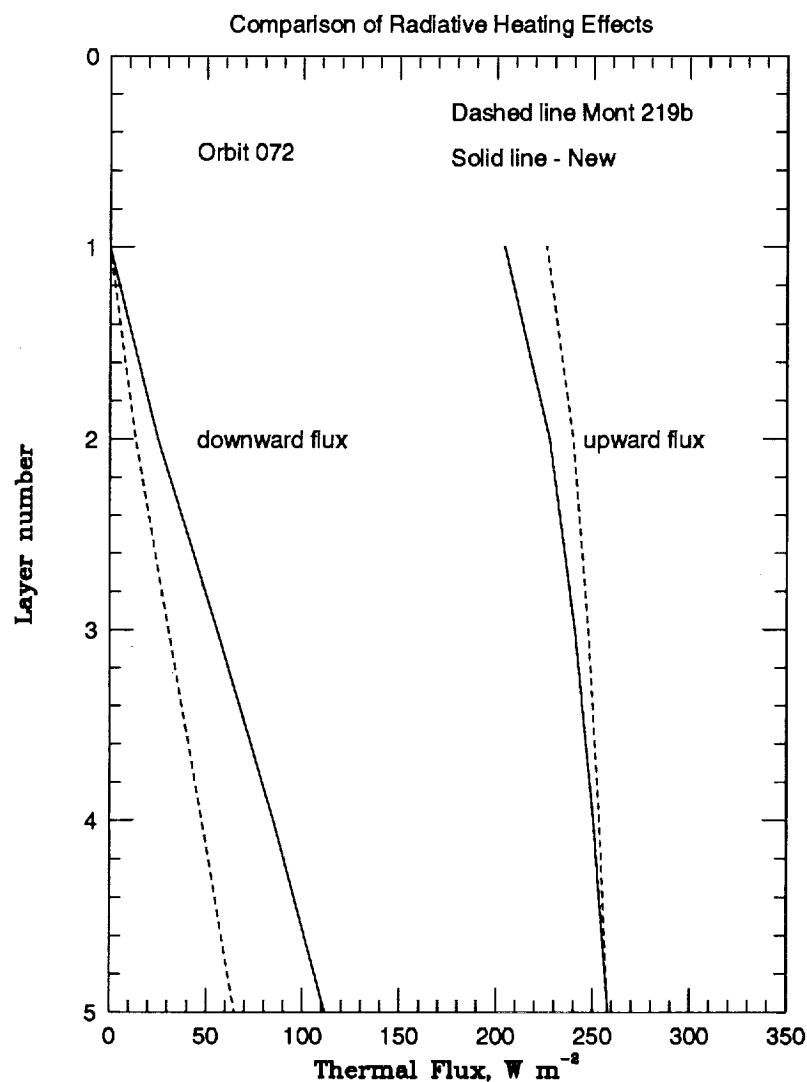


Figure 3.13: Fits to the selected brightness temperature spectra generated using the particle size distribution, optical properties, and temperatures assumed by Forget *et al.* [1997].



of slightly altering optical properties will be on the integrated fluxes. As a demonstration of the effects of our improved optical properties, we have calculated both upward and downward fluxes in the atmosphere for each orbit by integrating the upward and downward intensities from the multilayer radiative transfer code over all view angles and over all wavelengths. In Figure 3.14, we compare the fluxes resulting from our optical properties (solid lines) to those of montmorillonite (dotted lines). It is immediately obvious that the effect is large, with montmorillonite underpredicting the downward flux at the surface by nearly half in the dustier orbits and overpredicts the upward flux at the top of the atmosphere by nearly ten percent. Figure 3.15 shows the comparison over all orbits of the upward and downward fluxes.

**Figure 3.14: Upward and downward fluxes computed using current montmorillonite optical properties (solid lines) compared with those computed using the new optical properties presented in this thesis for dusty conditions such as those found during Mariner 9's orbit 8. The current model underpredicts the downwelling radiation at the surface by nearly half, and overpredicts the upwelling radiation at the top of the atmosphere by nearly ten percent.**



**Figure 3.15:** Upward and downward fluxes computed using current montmorillonite optical properties (stars) compared with those computed using the new optical properties presented in this thesis (X's) for all selected orbits. The current model underpredicts the downwelling radiation at the surface by up to nearly 50 radiation at the top of the atmosphere by up to nearly ten percent.

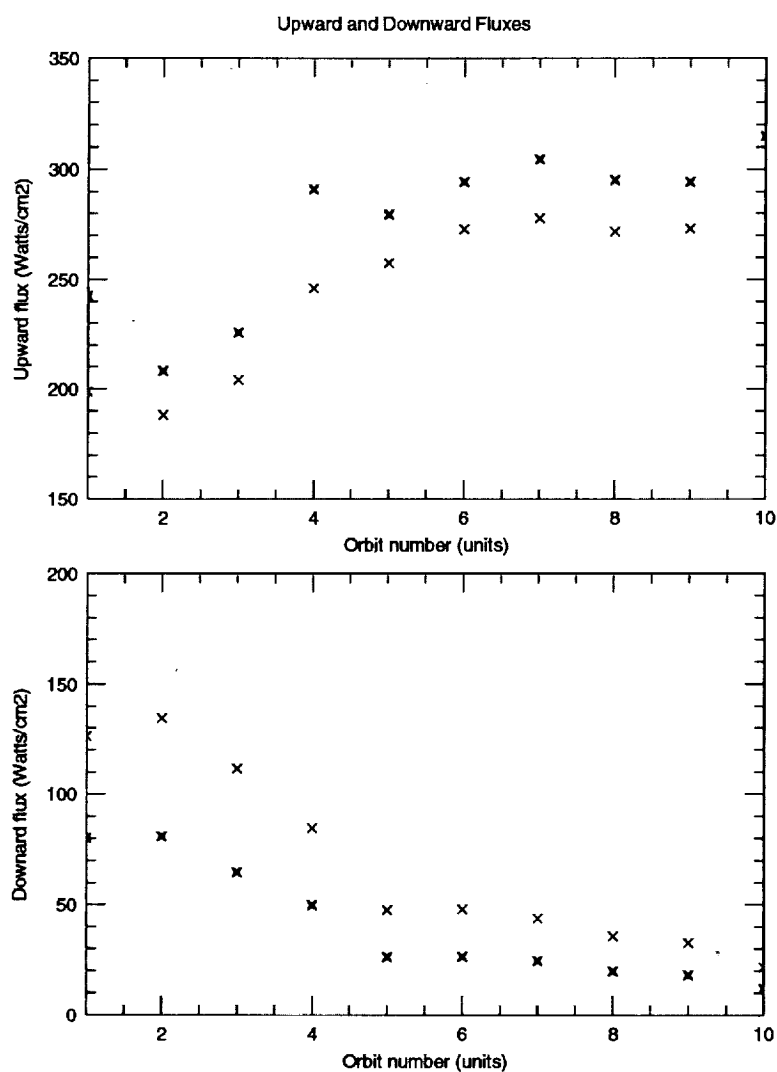


**Table 3.1: Orbit data computed using the Pollack *et al.* [1995] size distribution**

Spec	$\tau$	$\bar{\mu}$	$\mu$	$T_{\text{top}}$ , K	$T_{\text{bot}}$ , K	$T_{\text{surf}}$ , K	$r_m$	$\sigma$
1	1.339	0.500	0.417	214.177	243.746	271.877	0.660	0.642
2	1.292	0.500	0.904	199.792	259.488	260.417	0.660	0.642
3	0.904	0.500	0.969	196.730	258.875	265.273	0.660	0.642
4	0.739	0.500	0.387	191.079	246.290	282.057	0.660	0.642
5	0.292	0.500	0.996	179.595	249.974	276.924	0.660	0.642
6	0.270	0.500	0.982	178.460	255.760	280.085	0.660	0.642
7	0.320	0.500	0.527	174.716	245.766	282.262	0.660	0.642
8	0.270	0.500	0.505	168.652	241.217	279.393	0.660	0.642
9	0.208	0.500	0.980	168.652	241.217	280.000	0.660	0.642
10	0.085	0.500	0.974	169.684	240.538	282.710	0.660	0.642

**Table 3.2: Sensitivity of model to parameters, given by rms error (Kelvin) in brightness temperature over all wavenumbers and orbits.**

Param	Ave.	008	056	072	080	138	146	154	174H	174L	200
Baseline	1.15	2.31	1.15	1.17	1.43	0.76	0.82	1.23	1.08	0.94	1.23
$\tau$ +10%	1.45	1.47	1.51	1.48	3.27	0.86	0.85	2.12	1.36	0.85	1.13
$\tau$ -10%	1.53	3.82	1.23	1.24	1.50	0.91	0.99	0.86	1.54	1.17	1.35
$T_i$ +5 K	1.98	5.34	2.46	1.85	1.61	0.89	0.99	0.81	1.32	1.08	1.30
$T_i$ -5 K	1.66	2.23	2.73	2.10	3.23	0.86	0.84	1.87	1.21	0.87	1.17
$T_s$ +5 K	4.33	4.31	3.27	3.98	2.50	5.21	5.34	4.03	5.33	5.83	6.39
$T_s$ -5 K	4.11	2.04	3.96	4.54	4.59	5.19	5.12	5.66	4.61	4.87	4.67
$\sigma$ +10%	1.81	1.53	2.07	1.89	4.33	1.14	1.12	2.55	1.55	1.03	1.19
$\sigma$ -10%	1.95	5.23	1.10	1.14	2.38	0.82	0.90	0.91	1.93	1.15	1.34
$r_m$ +10%	1.37	1.57	1.66	1.53	2.71	0.92	0.95	1.78	0.96	0.95	1.19
$r_m$ -10%	1.42	3.74	0.96	1.04	1.18	0.73	0.81	0.81	1.45	1.02	1.28
$nr$ +10%	1.49	2.77	1.36	1.22	2.72	0.76	0.86	1.28	1.01	0.93	1.23
$nr$ -10%	1.44	3.14	1.38	1.37	1.73	0.88	0.87	1.60	1.39	1.00	1.22
$ni$ +10%	1.17	2.03	1.23	1.25	1.84	0.78	0.83	1.45	1.12	0.91	1.20
$ni$ -10%	1.18	2.64	1.11	1.13	1.11	0.76	0.83	1.02	1.11	0.98	1.26



**Table 3.3: Parameters used in various studies in the literature**

Study	Year	Optical properties	$r_{eff}$ $\mu\text{m}$	$v_{eff} r_m$ $\mu\text{m}$	$\sigma$ $\mu\text{m}$	
Toon	1977	Montmorillonite 219b	2.75	.4182	1.3	.548
Drossart	1991	?	1.24	.25	.709	.472
Moroz	1993	?	1.6	.25	?	?
Santee	1993	No scattering	.709	0.16	.5	.387
Pollack	1995	Montmorillonite 219b	1.85	0.51	0.66	0.642
Clancy	1995	Palagonite	1.8	0.8	.33	.387
Forget	1997	Mod. <u>montmorillonite</u>	2.75	.4182	1.3	.548
Ockert-Bell	1997	(visible)	1.85	0.51	0.66	0.42
Snook	1998	inverted	1.85	0.51	0.66	0.42

## 4. Conclusions

Our method of directly inverting thermal emission spectra of Mars to determine the optical properties, opacity, surface temperatures, and particle size distribution of the suspended Mars dust has been demonstrated to be successful in fitting the Mariner 9 data to an accuracy that exceeds the accuracy of the data itself. We have found that a particle size distribution with an effective radius of  $\tau_{\text{eff}} = 1.85\mu\text{m}$  and an effective variance of  $v_{\text{eff}} = 0.51$  enables convergence to realistic values for surface temperatures (260-281 K) and optical depth (1.34 - 0.18).